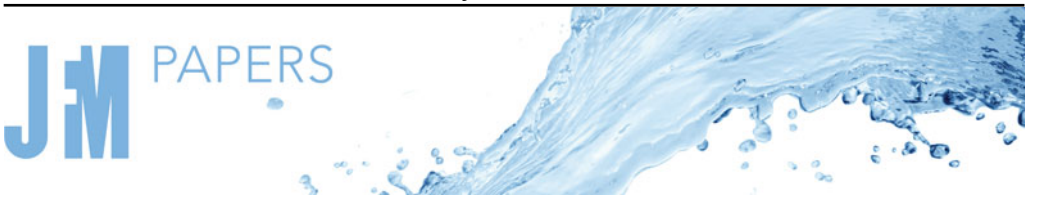
J. Fluid Mech. (2026), *vol.* 1041, A31, doi:10.1017/jfm.2026.11950



Quiescent core in turbulent channel flow with spanwise-uniform roughness

Jiahui Han[1,2,3], **Wen Zhang**[1,2,3,4], **Xue Chen**[1,2,3] **and Minping Wan**[1,2,3]

[1]Guangdong Provincial Key Laboratory of Turbulence Research and Applications, Department of Mechanics and Aerospace Engineering, Southern University of Science and Technology, Shenzhen, Guangdong 518055, PR China

[2]Guangdong-Hong Kong-Macao Joint Laboratory for Data-Driven Fluid Mechanics and Engineering Applications, Southern University of Science and Technology, Shenzhen, Guangdong 518055, PR China

[3]Shenzhen Key Laboratory of Complex Aerospace Flows, Department of Mechanics and Aerospace Engineering, Southern University of Science and Technology, Shenzhen 518055, PR China

[4]Advanced Institute for Ocean Research, Southern University of Science and Technology, Shenzhen 518055, PR China

Corresponding authors: Minping Wan, wanmp@sustech.edu.cn; Xue Chen, chenx3@sustech.edu.cn

(Received 18 February 2026 UTC; revised 17 July 2026 UTC; accepted 20 July 2026 UTC)

This study examines drag and outer-layer similarity in a rough-wall channel with spanwise-uniform bars at pitch-to-height ratios 6, 12 and 24, using direct numerical simulations at $Re_\tau = 395$. The quiescent core (QC) is detected via kernel density estimation of the streamwise velocity probability density function (PDF). The QC modal velocity remains nearly identical for rough and smooth walls, providing a basis for outer-layer similarity, whereas the exterior modal velocity shifts to lower values and broadens. Over rough walls, the QC becomes thinner, exhibits larger wall-normal excursions, and interrupts the centreline more frequently. These geometric changes alter the extent and stability of the highest-speed zone, increasing contact between the core and slower fluid in the roughness sublayer, and producing larger velocity jumps. Joint PDFs weighted by Reynolds shear stress indicate that strong shear at the QC boundary shifts momentum-carrying events towards larger amplitudes. Linear stochastic estimation shows that near-wall structures follow the roughness geometry, while structures at the QC boundary differ systematically across cases, becoming progressively more spatially compact as QC disruption intensifies. Overall, QC geometry and interfacial metrics appear to provide a compact, structure-informed framework for interpreting the non-monotonic drag variation and the partial breakdown of outer-layer similarity observed in the present configuration.

Key words: boundary layer structure, turbulence simulation, shear layer turbulence

© The Author(s), 2026. Published by Cambridge University Press.

https://doi.org/10.1017/jfm.2026.11950 Published online by Cambridge University Press

1. Introduction

1.1. *Rough-wall flows and outer-layer similarity*

Most wall-bounded flows of practical interest involve rough walls. Establishing a unified trend of drag with rough topography and the generality of outer-layer similarity remains ambiguous. The difficulty arises as drag can vary non-monotonically with roughness topography, and similarity in mean velocity does not necessarily imply similarity in second-order statistics for the same roughness surface. Furthermore, the connection to momentum-transport mechanisms has not been fully understood (Chung *et al.* 2021). In practice, the increase in frictional drag due to roughness is quantified by the roughness function ΔU^+, defined as the downward shift of the logarithmic mean velocity profile relative to a smooth wall (Clauser 1954). The logarithmic law is

$$U^+(y^+) = \frac{1}{\kappa} \ln y^+ + B, \tag{1.1}$$

where $U^+ = U/u_\tau$ and $y^+ = y\,u_\tau/\nu$, $u_\tau = \sqrt{\tau_w/\rho}$ is the friction velocity, ν is the kinematic viscosity, κ is the von Kármán constant, and B is the intercept.

The roughness function is conventionally estimated from the shift between smooth- and rough-wall profiles, which is approximately constant above the lower logarithmic region and throughout the outer layer:

$$\Delta U^+ \equiv U_s^+(y^+) - U_r^+(y^+), \tag{1.2}$$

with U_s^+ and U_r^+ denoting smooth- and rough-wall mean velocities, respectively. A common basis for using this single parameter is Townsend's outer-layer similarity hypothesis (Townsend 1976), which states that with adequate scale separation ($k \ll \delta$, where k denotes the roughness height, and δ denotes the boundary-layer thickness), the direct influence of roughness is largely confined within the inner region, whereas the outer layer, when normalised by u_τ, becomes approximately independent of wall condition (for summaries, see Raupach *et al.* 1991; Jiménez 2004; Chung *et al.* 2021; Cheng *et al.* 2024).

Against this background, two issues complicate the generalisation of ΔU^+ across roughness geometries. First, ΔU^+ does not vary monotonically with element density. In boundary-layer measurements over block arrays, Vanderwel & Ganapathisubramani (2019) reported that drag increased when element spacing was reduced from very sparse conditions, which attained a maximum at intermediate frontal solidity, and the drag decreased again when mutual sheltering became dominant at higher element densities. A similar trend was found for sinusoidal surfaces by MacDonald *et al.* (2016), who varied roughness density at fixed height, and observed a peak in ΔU^+ at intermediate effective slopes, followed by a decline as density increased further. Such non-monotonic behaviour of drag versus element spacing is consistent with the observation by Chung *et al.* (2021) in which element-scale form drag competes with inter-element sheltering or skimming. Second, the generality of outer-layer similarity remains ambiguous. While Squire *et al.* (2016) showed that at sufficiently high Reynolds number and small k/δ, the mean velocity can be represented by a shifted logarithmic profile, many studies (Flack & Schultz 2014) report elevated outer-layer Reynolds stresses relative to smooth walls even when the mean profile is approximately similar. Therefore, the non-monotonic dependence of ΔU^+ on density, and the potential divergence between mean and second-order similarity, indicate that the link between roughness geometry, coherent structures and momentum transport is not yet fully understood.

https://doi.org/10.1017/jfm.2026.11950 Published online by Cambridge University Press

These difficulties become more prominent for two-dimensional (2-D), spanwise-uniform roughness, a rough-wall configuration widely investigated since Perry *et al.* (1969) put forward the classical k-type/d-type roughness classification (Tani 1987). Subsequently, the numerical study by Leonardi *et al.* (2003) quantified how the streamwise pitch-to-roughness-height ratio p/k governs the drag response for rough-wall flows over transverse bars, where p denotes the streamwise centre-to-centre spacing of the bars. A recent parametric investigation of p/k by Kong *et al.* (2023) indicates that for bar arrays, ΔU^+ increases as the pitch-to-height ratio p/k is reduced from large values, peaks near $p/k \approx 8$ under the conditions surveyed, then decreases as the sheltering effect strengthens with decreasing pitch. They also observed that the redistribution of energy towards larger scales is most evident near the p/k range where ΔU^+ attains its maximum. Meanwhile, the outer layer exhibited amplified coherent structures, with strengthened large- and very-large-scale motions, and elevated turbulence intensities relative to smooth walls (Jin *et al.* 2015). As the spacing is reduced further towards very dense configurations, the flow tends to skim over the crests, and the element spacing becomes the primary control on ΔU^+ for deep bar arrays (MacDonald *et al.* 2018). Unlike various three-dimensional (3-D) roughness topographies, the spanwise blockage of 2-D bars causes sheltering and skimming layers to redevelop behind each element, leading to more frequent streamwise variations in the roughness sublayer thickness. This repeated re-formation may contribute to the difficulty of achieving outer-layer similarity, particularly for second-order statistics. Measurements over 2-D bars report larger outer-layer structures and departures from similarity (Volino *et al.* 2009, 2011), whereas studies at higher Reynolds number and smaller k/δ indicate a conditional recovery of similarity (Krogstad & Efros 2012; Flack & Schultz 2014). Hence it is evident that spanwise-uniform bars tend to deviate from outer-layer similarity, which suggests that the overall drag prediction of flows over 2-D roughnesses should be tied to how rough-wall geometry affects momentum exchange and the associated coherent structures (Volino *et al.* 2009; Han *et al.* 2026).

1.2. *Uniform-momentum zone, quiescent core and internal shear layers*

The existence of uniform-momentum zones (UMZs) in wall-bounded flows was first reported by Adrian *et al.* (2000), who identified large regions convecting downstream with relatively small velocity discrepancies. These zones inherently yield distinct peaks on the probability density function (PDF) of the instantaneous streamwise velocity. These regions are demarcated by thin layers of strong local shearing resulting from concentrated spanwise vorticity, and their threshold velocities are estimated as local minima between adjacent peaks on the PDF. Studies on smooth-wall-bounded flows have shown that these internal shear layers (ISLs) are responsible for most of the velocity and temperature propagation from the wall towards the outer region by intensified Q2 ejections and Q4 sweep activities across the ISL (Kwon *et al.* 2014; de Silva *et al.* 2017; Chen *et al.* 2020).

The UMZ with the highest modal velocity, hereafter the quiescent core (QC), occupies the central region of the channel or pipe, bounded above and below by ISLs that form the core boundary (Kwon *et al.* 2014; Yang *et al.* 2016). The topology of the QC and its boundary are of great interest as their tortuosity, meandering, thinning and thickening are manifestations of the large- and very-large-scale motions associated with interfacial momentum, mass and heat transfer (de Silva *et al.* 2017; Kevin *et al.* 2019; Chen *et al.* 2020; Heisel *et al.* 2020). Moreover, conditional averages around the ISLs revealed the dynamics of the entrainment of near-wall fluids across the ISL into the outer region induced by strong local Q2 and Q4 motions (Gul *et al.* 2020; Chen *et al.* 2021). Therefore, the statistical characteristics of the UMZ/QC and their bounding interface provide a novel

https://doi.org/10.1017/jfm.2026.11950 Published online by Cambridge University Press

and intuitive measure of the influence of rough-element configuration imposed on the outer-layer similarity and underlying mechanism from a dynamical structural viewpoint.

In recent years, analyses of the UMZ/QC and ISL have thereby been exploited in smooth-wall studies to evaluate the influence on multi-scale coherent structures due to flow acceleration (Guerrero *et al.* 2023), free-stream turbulence (Hearst *et al.* 2021), superhydrophobic surfaces (Wang *et al.* 2023), unstably stratified wall turbulence (Salesky 2023) and compressibility in supersonic flow (Wang *et al.* 2024). Very recently, Zhang *et al.* (2026) examined UMZ statistics in rough-wall boundary layers, and confirmed broad outer-layer similarity, yet the QC behaviour in internal flows with systematically varied 2-D roughness density remains unaddressed.

While existing studies have clarified UMZ/QC statistics in smooth-wall flows, and more recently in rough-wall boundary layers (Zhang *et al.* 2026), a quantitative link between roughness topography, outer-layer similarity, interface dynamics and ΔU^+ in internal flows remains to be established. In this context, the QC and its interface offer compact, structure-informed metrics that help to interpret non-monotonic drag and outer-layer stress trends in terms of geometric deformation and intermittency of the highest-speed zone. The present study conducts in-depth analyses of the QC in flows over transverse-bar roughness, linking distinctive QC characteristics to the momentum transport driven by wall roughness, and shedding light on the generality of outer-layer similarity in rough-wall flows.

The paper is organised as follows. Section 2 describes the numerical methodology and roughness topographies. Section 3 presents bulk statistics, including the frictional drag response and an assessment of conditional outer-layer similarity. The QC identification over rough surfaces is addressed in § 4, which elaborates on the PDF-based QC detection with kernel density estimation. In § 5, QC geometry and intermittency are investigated in relation to interfacial dynamics. Section 6 analyses conditional averages across the QC boundary, and identifies coherent structures using linear stochastic estimation with links to interfacial momentum transfer mechanisms in wall-bounded flows. Section 7 provides a concluding discussion.

2. Numerical method

2.1. *Direct numerical simulations*

Direct numerical simulations (DNS) of smooth- and rough-wall channel flow (figure 1) were performed by solving the incompressible Navier–Stokes equations in dimensional form in Nek5000 (Fischer *et al.* 2008) as

$$\frac{\partial u_i}{\partial x_i} = 0, \tag{2.1}$$

$$\frac{\partial u_i}{\partial t} + u_j \frac{\partial u_i}{\partial x_j} = -\frac{1}{\rho}\frac{\partial P}{\partial x_i} + \nu \frac{\partial^2 u_i}{\partial x_j^2} + f_i, \tag{2.2}$$

where u_i denotes the velocity components. A constant streamwise body force $f_i = (f_x, 0, 0)$ is applied, equivalent to a uniform pressure gradient $f_x = -(1/\rho)\,\partial P/\partial x$. For the smooth-wall case, the domain size is $L_x \times L_y \times L_z = 12h \times 2h \times 6h$, and periodic boundary conditions are imposed in the streamwise (x) and spanwise (z) directions, with no-slip conditions on all solid surfaces. The equations are solved using a semi-implicit scheme in which the nonlinear terms are advanced by third-order extrapolation (EXT3), and the viscous terms by third-order backward differentiation (BDF3). Spatial

https://doi.org/10.1017/jfm.2026.11950 Published online by Cambridge University Press

Case	Re_τ	p/k	k	$L_x \times L_y \times L_z$	N_e	Δx^+	Δy^+	Δz^+	ΔU^+
P24	—	24	—	—	141 372	[2.82, 11.85]	[0.11, 11.85]	7.9	7.83
P12	395	12	0.1	$12 \times 2.2 \times 6$	158 760	[2.82, 12.90]	[0.11, 11.85]	7.9	9.61
P06	—	6	—	—	183 204	[2.82, 10.72]	[0.11, 11.85]	7.9	9.32
SM	—	—	—	$12 \times 2 \times 6$	129 500	12	[0.11, 9.59]	6.8	—
P24H	590	24	0.1	$12 \times 2.2 \times 6$	620 240	[3.60, 7.37]	[0.12, 10.3]	7.4	—

Table 1. Summary of simulation parameters, where N_e denotes the number of high-order elements. Domain sizes are normalised by h, and grid spacings are in wall units.

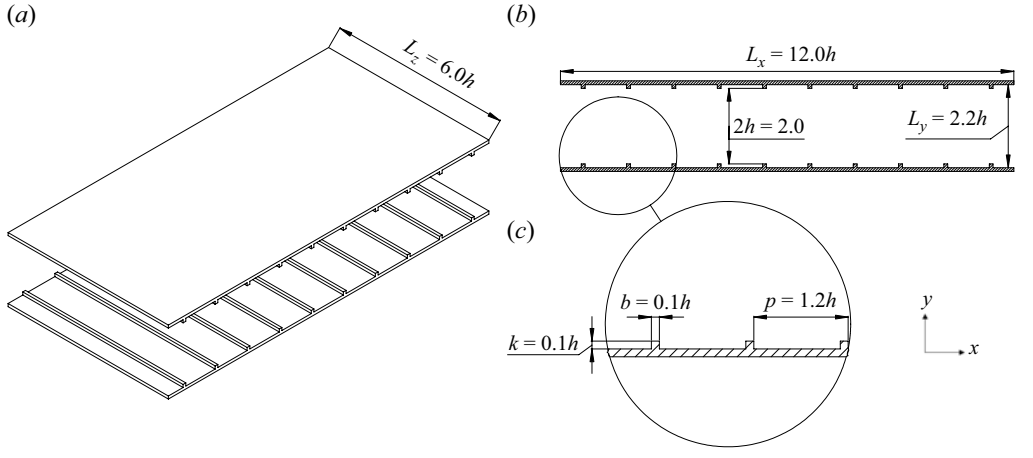


Figure 1. Illustration of the rough-wall configuration with case P12: (*a*) 3-D view; (*b*) streamwise-wall-normal (x–y) view; (*c*) local roughness unit with $k = b = 0.1h$ and pitch $p = 1.2h$ (bar width included).

discretisation employs curvilinear hexahedral spectral elements with an inf–sup stable $P_N - P_{N-2}$ approximation, where degree-7 polynomials are used for velocity, and degree-5 for pressure. Grid spacings are summarised in table 1, and the first off-wall point has $\Delta y^+ \approx 0.11$ for both the smooth- and rough-wall cases.

2.2. *Roughness configuration*

The simulation campaign comprises four rough-wall cases and one smooth-wall reference. Three cases, P06, P12 and P24, at $Re_\tau = 395$ correspond to pitch-to-height ratios $p/k = 6$, 12 and 24, respectively, and are designed to isolate the effect of roughness geometry at fixed Reynolds number. A fourth case, P24H, repeats the P24 geometry at $Re_\tau = 590$ to examine the sensitivity of the QC statistics to Reynolds number. The rough-wall channel comprises spanwise-continuous, 2-D transverse bars of height and width $k = b = 0.1h$ in a domain of size $L_x \times L_y \times L_z = 12h \times 2.2h \times 6h$. Accordingly, the number of streamwise pitch repetitions is $N_p = L_x/p$, with $N_p = 20$ (P06), $N_p = 10$ (P12) and $N_p = 5$ (P24, P24H). To enhance resolution near the roughness, the streamwise and spanwise mesh spacings were refined locally. In the streamwise direction, two high-order elements are used across one roughness unit (one pitch), yielding 16 Gauss–Lobatto–Legendre velocity points per unit.

https://doi.org/10.1017/jfm.2026.11950 Published online by Cambridge University Press

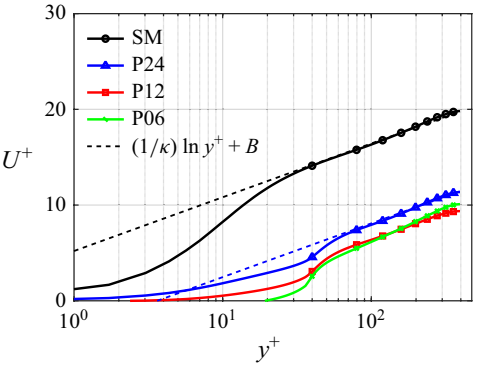


Figure 2. Mean velocity U^+ versus y^+ for the smooth wall and rough walls with $p/k = 6$, 12, 24. The black dashed line denotes $U^+ = (1/\kappa)\ln y^+ + B$, where $\kappa = 0.41$ is the von Kármán constant, and $B = 5.2$ is the intercept.

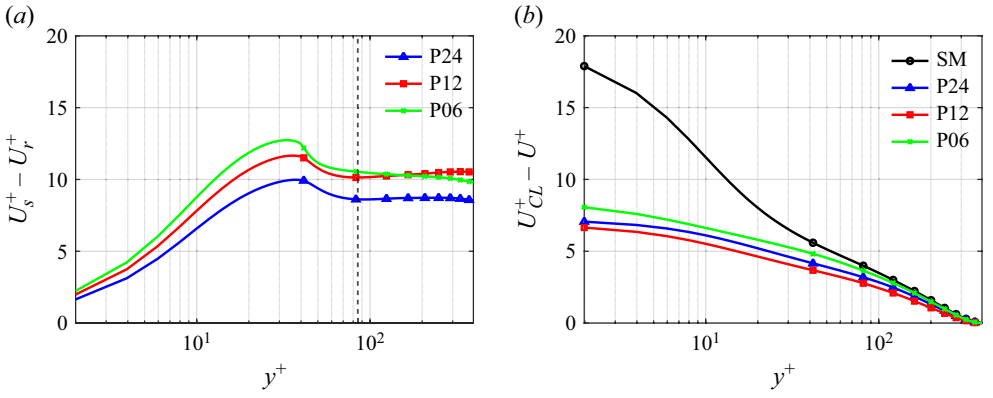


Figure 3. (*a*) Smooth–rough difference $U_s^+ - U_r^+$ versus y^+ on semi-logarithmic scales. (*b*) Velocity defect $U_{CL}^+ - U^+$. The outer-region plateau in (*a*) for $y^+ \gtrsim 100$ is used to determine ΔU^+.

3. Drag and outer-layer similarity

The mean streamwise velocity U^+ is examined to assess roughness effects on drag and the outer-layer similarity. As shown in figure 2, the smooth-wall profile follows the logarithmic law, whereas all rough-wall profiles exhibit the expected downward shift ΔU^+, together with clear logarithmic regions. Among the rough-wall cases, the U^+ profile of P24 ($p/k = 24$) is notably parallel to the smooth-wall curve (SM) within the logarithmic range, whereas P12 and P06 exhibit a modest offset in slope. The presence of logarithmic regions across all rough cases is consistent with conditional outer-layer similarity, while the changes in slope for P12 and P06 indicate the effect of the rough wall on the outer layer relative to the smooth wall.

To assess the roughness function and the associated drag, the smooth–rough velocity difference $U_s^+ - U_r^+$ is evaluated in figure 3(*a*). In the outer region ($y^+ \gtrsim 100$), the profiles approach a plateau, and here, ΔU^+ is estimated as its mean value over this region, listed in table 1. Here, ΔU^+ exhibits a non-monotonic decrease with increasing roughness density, p/k: P24 yields the smallest ΔU^+, and P12 the largest, and P06 is comparable to P12. Such a non-monotonic dependence of ΔU^+ on p/k is consistent with the observation of Volino *et al.* (2009, 2011) and Flack & Schultz (2014) for transverse bar roughness.

https://doi.org/10.1017/jfm.2026.11950 Published online by Cambridge University Press

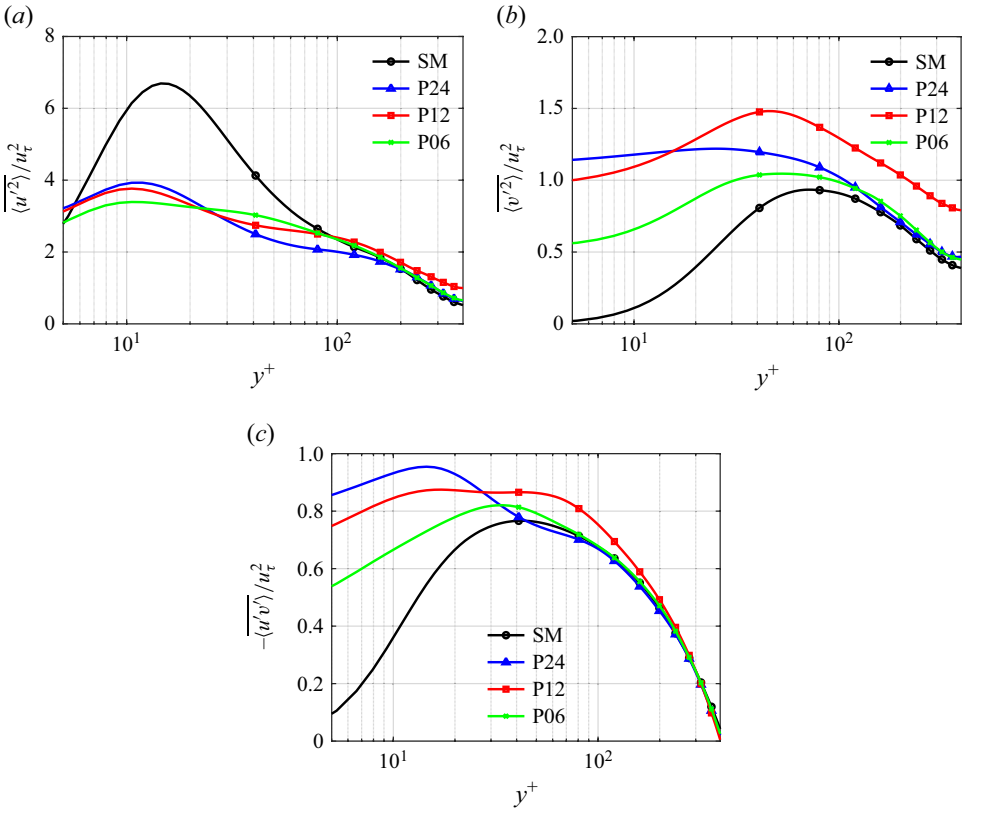


Figure 4. Reynolds stresses versus y^+: (*a*) $\overline{\langle u'^2\rangle}/u_\tau^2$, (*b*) $\overline{\langle v'^2\rangle}/u_\tau^2$ and (*c*) $-\overline{\langle u'v'\rangle}/u_\tau^2$, for the smooth wall and rough walls with $p/k = 6$, 12, 24.

The centreline velocity deficit, $U_{CL}^+ - U^+$, is shown in figure 3(*b*). All rough-wall profiles exhibit a smaller deficit than the smooth wall. In the outer region, P24 and P06 approximately collapse onto the smooth-wall data, whereas P12 departs modestly from this group, consistent with its larger ΔU^+. Taken together with the slope changes noted above, these results suggest that the fitted logarithmic slope and intercept both depart from their smooth-wall counterparts and vary with p/k. Similar modifications of the fitted logarithmic-law parameters have been reported for 2-D bar roughness by Volino *et al.* (2009) and Krogstad & Efros (2012).

Figure 4 shows the Reynolds normal stresses $\overline{\langle u'^2\rangle}/u_\tau^2$ and $\overline{\langle v'^2\rangle}/u_\tau^2$, together with the Reynolds shear stress $-\overline{\langle u'v'\rangle}/u_\tau^2$. Here, the prime denotes the fluctuation about the local time-averaged velocity, and the angle brackets denote spatial averaging. The quantities shown in figure 4 therefore contain only the Reynolds stress components, and do not include the dispersive stresses associated with spatial variations of the time-averaged flow. The P12 case departs from both the smooth wall and the other rough cases for both components, in which the deviation is particularly pronounced in the wall-normal intensity $\overline{\langle v'^2\rangle}/u_\tau^2$. The elevation of $\overline{\langle v'^2\rangle}/u_\tau^2$ in case P12 suggests substantially intensified wall-normal turbulent motions in the outer region at this pitch-to-height ratio. In a parametric DNS study of transverse-bar roughness, Leonardi *et al.* (2004) showed that as the element separation increases, wall-normal motions become increasingly important and

https://doi.org/10.1017/jfm.2026.11950 Published online by Cambridge University Press

reach their maximum intensity in configurations with larger drag, where intense ejections ($v' > 0$) develop at the plane of the crests, and interact with the overlying flow. This observation provides qualitative context for the elevated $\langle\overline{v'^2}\rangle/u_\tau^2$ in P12, although the mechanism responsible for its persistence into the outer region remains to be established. The corresponding Reynolds shear stress $-\langle\overline{u'v'}\rangle/u_\tau^2$ is also elevated in the near-wall and lower logarithmic regions, indicating intensified turbulent momentum transport in the cases most strongly affected by wall-normal motions. Evidence in structural perspective of how these motions are organised, with links to the QC interface statistics, is in the next section.

The slope changes in U^+ and the departures in $U_{CL}^+ - U^+$ and outer-layer intensities indicate that the mean velocity profile features a logarithmic region for which both the fitted slope and intercept vary with p/k, alongside variations in the magnitude of outer-layer turbulence fluctuation. The drag varies non-monotonically with p/k (P24 smallest, P12 largest, P06 comparable to P12), and P12 exhibits elevated outer-layer intensities – most notably in $\langle\overline{v'^2}\rangle/u_\tau^2$. To interpret how these departures arise, and what they imply for outer-layer structural organisation, the latter part of this study investigates the QC and the core interface by quantifying the spatial characteristics of the QC geometry (its thickness, centre position and intermittency as functions of p/k), and the Q2/Q4 event population across the QC boundary, thereby providing a structure-informed interpretation for the observed deviations and the non-monotonic ΔU^+.

4. Core identification

4.1. *The QC identification in the instantaneous field*

The UMZs are identified following Adrian *et al.* (2000) by constructing the PDF of the instantaneous streamwise velocity normalised by the centreline velocity u/U_{CL}, within a limited 3-D spatial domain (de Silva *et al.* 2016; Chen *et al.* 2020). Peaks of the PDF correspond to separate zones with modal velocities u_m, and the local minimum between adjacent peaks defines the interfacial threshold u_k (de Silva *et al.* 2016, 2017). The PDF method is sensitive to the bin width and peak-recognising schemes (Chen *et al.* 2021), and for robustness, a KDE of the PDF is employed following Fan *et al.* (2019). The details on the UMZ identification method are provided in Appendix A.

Figure 5 illustrates the procedure using a snapshot from the smooth-wall case. The PDF of u is computed from a limited 3-D domain with window size $l_x/h = 2$ in the streamwise direction, and $l_z/h = 0.5$ in the spanwise direction. In figure 5(*a*), two modal velocities (peaks) are identified from the KDE, which correspond to the highest-speed QC (UMZ with the highest modal velocity) with $u_{m,1} \approx 0.96\,U_{CL}$, and the adjacent lower-speed zone with $u_{m,2} \approx 0.84\,U_{CL}$. The interfacial threshold is given by the valley between peaks, $u_k \approx 0.88\,U_{CL}$. Figure 5(*b*) displays a 2-D slice of the windowed domain used in figure 5(*a*), in which the contour line encloses the QC at the given u_k.

4.2. *Selection of the identification region*

The PDF-based identification of UMZs is sensitive to the spatial window from which the velocity distribution is constructed (de Silva *et al.* 2016). Prior studies often used short streamwise extents (e.g. $l_x \approx 0.25\,h$) to resolve UMZs travelling at lower modal velocities, which are typically thinner and thus contribute less prominent PDF peaks (de Silva *et al.* 2016, 2017; Asadi *et al.* 2022). On the other hand, to identify the QC that occupies almost half of the flow domain around the centreline, a statistically converged distribution is required; streamwise windows of order $\mathcal{O}(h)$ (e.g. $l_x \approx 1.2\,h$ in Kwon *et al.* 2014) were

https://doi.org/10.1017/jfm.2026.11950 Published online by Cambridge University Press

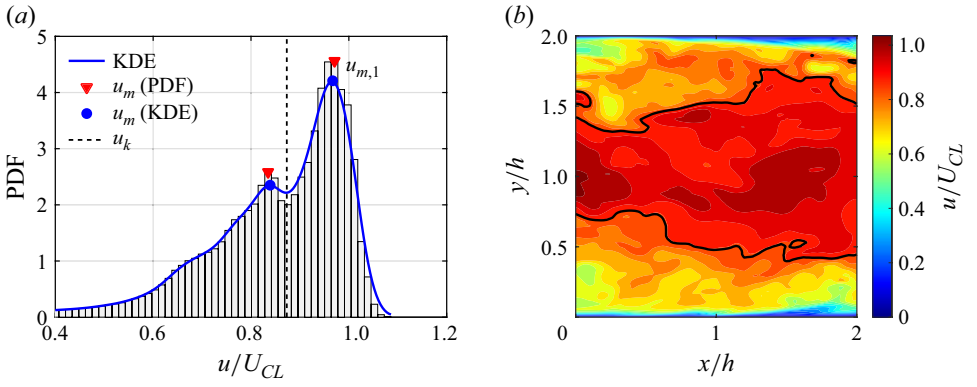


Figure 5. The UMZ identification for a representative SM snapshot using a 3-D window of $l_x/h = 2.0$ and $l_z/h = 0.5$. (*a*) The KDE-based PDF of u/U_{CL}; symbols mark modal velocities (u_m) and the interfacial threshold (u_k). (*b*) A 2-D slice of the instantaneous field; the black contour denotes $u_k \approx 0.88\,U_{CL}$.

found to be robust for planar (particle image velocimetry) measurements. Leveraging 3-D DNS fields, the present study performs the identification in 3-D windows, following the volumetric approach used in internal flows such as pipes (Chen *et al.* 2020; Chen *et al.* 2021).

In figure 6, a sensitivity analysis is conducted by varying the window extents over $1.0 \le l_x/h \le 6.0$ in the streamwise direction, and $0.1 \le l_z/h \le 3.0$ in the spanwise direction. This figure presents the distribution of the identified threshold u_k/U_{CL} as a scatter plot to visualise how the threshold responds to different combinations of streamwise and spanwise window sizes. A threshold u_k is deemed valid if the KDE distribution exhibits two separate peaks with a distinct intermediate valley. In such a scenario, u_k is defined as the velocity corresponding to the local minimum between the two peaks, which indicates a sharp velocity jump, i.e. a thin shear layer that serves as the boundary demarcating the QC from the exterior zone (de Silva *et al.* 2016; Chen *et al.* 2020). By contrast, if the KDE curve is unimodal, which is typically observed amid strong sweep or ejection events, without a discernible valley, then no valid u_k is retrieved under the given sampling window size (see Appendix A). With the histogram-based PDF method, as shown in figure 6(*a*), a valid u_k is obtained mainly for relatively small windows. Using KDE, as shown in figure 6(*b*), a valid u_k is recovered over a broader range, and the resulting map of u_k/U_{CL} displays a stratified dependence on the window size. Small (l_x, l_z) yields $u_k/U_{CL} \to 1$, increasing l_z drives $u_k/U_{CL} \to 0.95$, and larger l_x further reduces u_k/U_{CL} towards 0.9.

The spanwise dependence of u_k matches the spatial extent of large-scale motions. Figure 7 shows an instantaneous z–y plane of the streamwise velocity with the contour of $u/U_{CL} = 0.95$. The QC boundary exhibits spanwise intermittency with characteristic widths of order $0.5h$–$1.5h$, and streamwise extents of order h–$3h$ (Pope 2000). Revisiting figure 6(*b*), $u_k/U_{CL} \approx 0.95$ is recovered precisely when the window spans these large-scale motions, indicating that the $0.95\,U_{CL}$ threshold is not arbitrary but tied to the geometry of dominant outer-layer motions.

To demonstrate convergence of the window size selection, figure 8 shows the variation of $(u_{m,1}, u_{m,2}, u_k)$ with l_z/h at fixed $l_x/h = 2$, and with l_x/h at fixed $l_z/h = 0.5$ (KDE-based identification). For both l_x and l_z, u_k/U_{CL} stabilises to 0.95 once the window spans $l_z/h \gtrsim 0.5$ and $l_x/h \gtrsim 2$. Based on these trends, a standard window of $l_x/h = 2$ and $l_z/h = 0.5$ is adopted henceforth.

https://doi.org/10.1017/jfm.2026.11950 Published online by Cambridge University Press

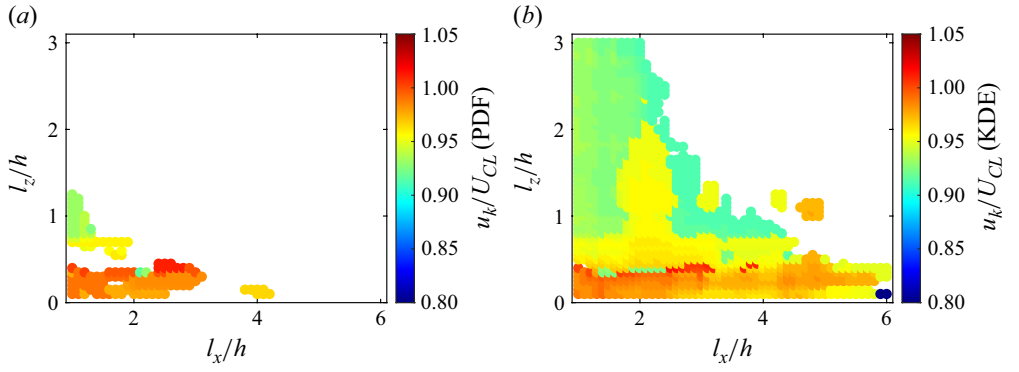


Figure 6. Sensitivity of the identified threshold u_k/U_{CL} to streamwise and spanwise window sizes for the SM case. Window sizes are varied across $l_x/h \in [1.0, 6.0]$ (streamwise) and $l_z/h \in [0.1, 3.0]$ (spanwise) to determine the interval of window dimensions that enables stable identification of the target threshold u_k/U_{CL}. Results from (*a*) the histogram-based PDF method, and (*b*) the KDE method.

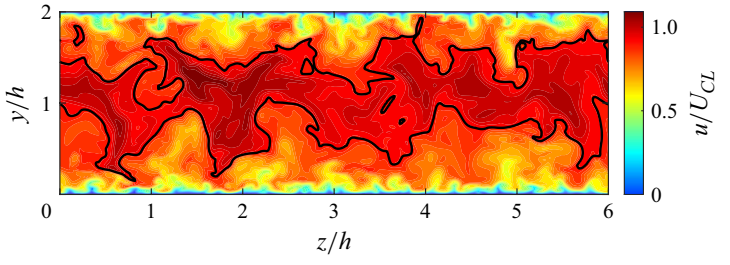


Figure 7. Instantaneous contour of u/U_{CL} in a z–y plane for the SM case. The solid black line shows the QC boundary defined at the threshold $u/U_{CL} = 0.95$.

4.3. *Determination of a QC boundary*

With the standard window, the KDE identification is applied across the domain with spanwise sliding (adjacent windows offset by five grid points). Following Asadi *et al.* (2022), figure 9 plots the distributions of the highest modal velocity $u_{m,1}$ and the second-highest modal velocity $u_{m,2}$ separately, where both are the KDE-peak velocities as defined in § 4.1, aggregated from all sliding-window analyses across the domain. Table 2 summarises the statistically converged modal velocities ($U_{m,1}$ for the QC, and $U_{m,2}$ for the adjacent zone, both derived by analysing the probability densities of their individual counterparts $u_{m,1}$ and $u_{m,2}$ from each sampled window), the robust threshold U_k (obtained similarly from the individual u_k across all windows) defined at the valley between modes, and the standard deviation σ_2 of the second mode.

The QC modal velocity $U_{m,1}$ remains nearly invariant (within $\pm 2\,\%$ of U_{CL}) across cases, whereas $U_{m,2}$ is strongly affected by roughness: compared with the SM value $U_{m,2}/U_{CL} \approx 0.93$, $U_{m,2}$ decreases to 0.89 U_{CL} (P24), 0.83 U_{CL} (P12) and 0.82 U_{CL} (P06). The broadening of the $u_{m,2}$ distribution is quantified by σ_2. The decrease and broadening of $U_{m,2}$ are consistent with the trend of the drag inferred from ΔU^+, and imply enhanced intermittency of the non-core region over rough walls, which is evaluated in § 5.

As shown in figure 9 and table 2, the QC interface threshold derived from the PDF of u_m yields $U_k/U_{CL} \approx 0.93$ (P24), $U_k/U_{CL} \approx 0.90$ (P12) and $U_k/U_{CL} \approx 0.91$ (P06), slightly

https://doi.org/10.1017/jfm.2026.11950 Published online by Cambridge University Press

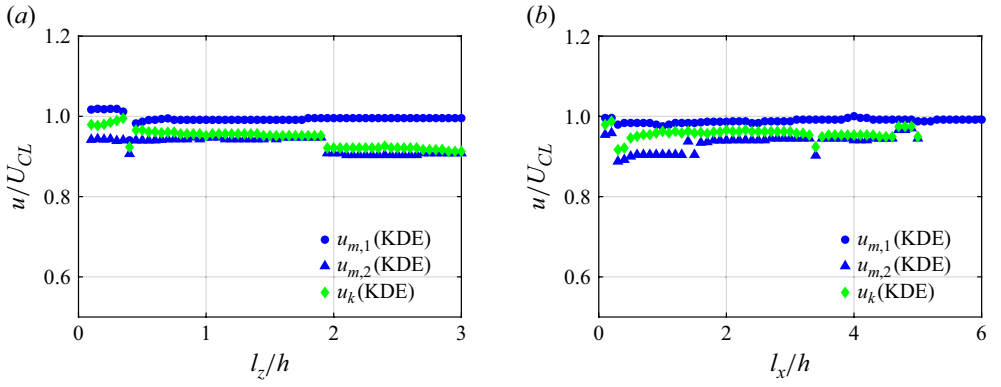


Figure 8. Convergence of modal velocities u_m and interface threshold velocity u_k using KDE in the SM case: (*a*) variation with l_z/h at fixed $l_x/h = 2$; (*b*) variation with l_x/h at fixed $l_z/h = 0.5$.

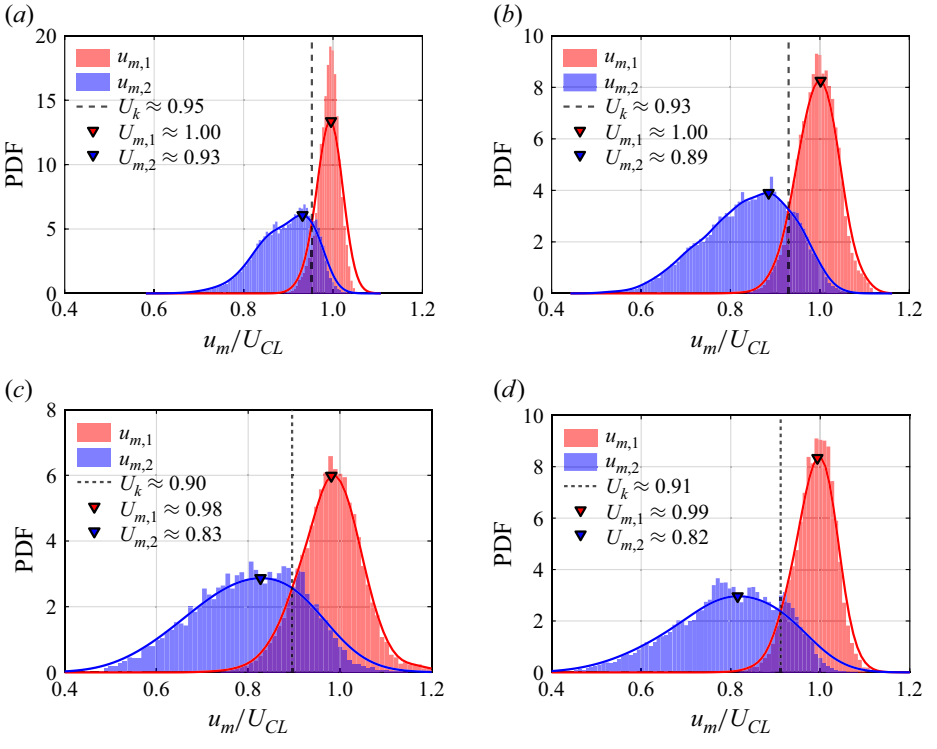


Figure 9. Aggregated PDFs of the first ($u_{m,1}$, red) and second ($u_{m,2}$, blue) modal velocities for (*a*) the SM case, and the rough-wall cases (*b*) P24, (*c*) P12, and (*d*) P06. The histograms represent the collected data from all sampled domains, while the solid lines are the corresponding KDE fits. The statistical modal velocities ($U_{m,1}$ and $U_{m,2}$) are marked by triangles at the peaks of the KDE curves. The dashed vertical line indicates the identified threshold velocity U_k.

lower than the SM value $U_k/U_{CL} = 0.95$, since these values are influenced by the widening and displacement of $U_{m,2}$ (see σ_2 in table 2). For direct comparison, and to target the QC boundary tied to the first mode, a fixed threshold $U_k/U_{CL} = 0.95$ is adopted across all flow cases.

https://doi.org/10.1017/jfm.2026.11950 Published online by Cambridge University Press

Case	$U_{m,1}/U_{CL}$	$U_{m,2}/U_{CL}$	U_k/U_{CL}	σ_2
P24	1.00	0.89	0.93	0.10
P12	0.98	0.83	0.90	0.11
P06	0.99	0.82	0.91	0.12
SM	1.00	0.93	0.95	0.06
P24H	1.00	0.86	0.93	0.11

Table 2. Summary of the identified modal velocities ($U_{m,1}$, $U_{m,2}$), the corresponding threshold velocity (U_k), and the standard deviation σ_2 of $u_{m,2}$ for all cases.

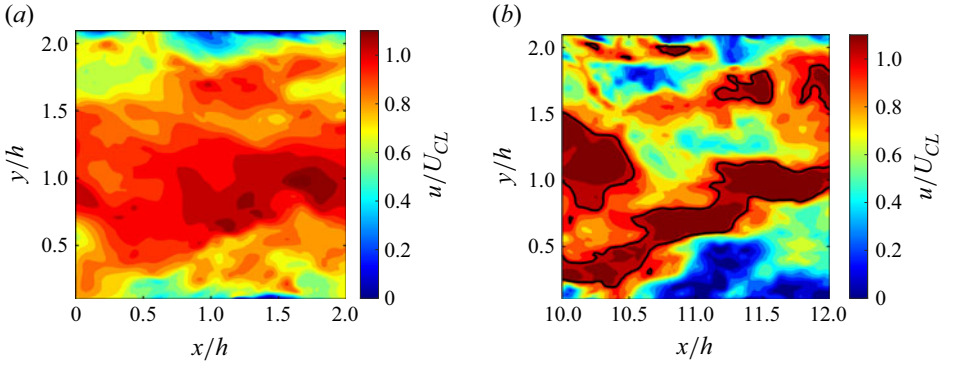


Figure 10. Examples of instantaneous events that challenge modal separation. (*a*) Sweep-dominated field (P24) in which a distinct low-speed mode is absent. (*b*) Ejection-dominated field (P12) in which the identified u_k deviates from its statistical value.

Furthermore, the larger σ_2 for rough walls implies that within a given window, the instantaneous distribution becomes less bimodal and exhibits a marked shift of $U_{m,2}$ towards lower modal velocities, typically during strong sweep or ejection events. Figure 10 depicts such dynamics in the instantaneous fields: in figure 10(*a*) for the P24 case, a sweep-dominated field suppresses the low-velocity peak and precludes a distinct u_k, i.e. no QC boundary can be established, whereas in figure 10(*b*) for the P12 case, an ejection-dominated field shifts the valley and yields u_k that deviates significantly from the mean U_k. This observed difference in the core topology is consistent with the broader $u_{m,2}$ PDFs and increased intermittency over rough walls (Volino *et al.* 2009, 2011).

5. Geometric characteristics of the QC

Figure 11 displays the instantaneous 3-D isosurfaces of the QC defined by the fixed threshold $U/U_{CL} = 0.95$, providing an intuitive comparison of the outer-layer structural organisation between the smooth wall and the rough wall with 2-D roughness. In figure 11(*a*), the QC boundary in the SM flow exhibits long streamwise coherence. The QC boundary is coloured by its elevation from the centreline d_c, which visually reveals the undulations of the upper and lower boundaries consistent with the organisation of very-large-scale motions, as reported in Kwon *et al.* (2014) and Chen *et al.* (2020). In the x–y slices extracted at $z/h = 3$, the 2-D contour of the QC shows relatively modest streamwise variation of the QC thickness, while the y–z plane ($x/h = 6$) reveals spanwise-arranged packet-like fragments. Upward concavities of the isosurface (displacements away from the wall) indicate ejection events, while downward protrusions (towards the wall)

https://doi.org/10.1017/jfm.2026.11950 Published online by Cambridge University Press

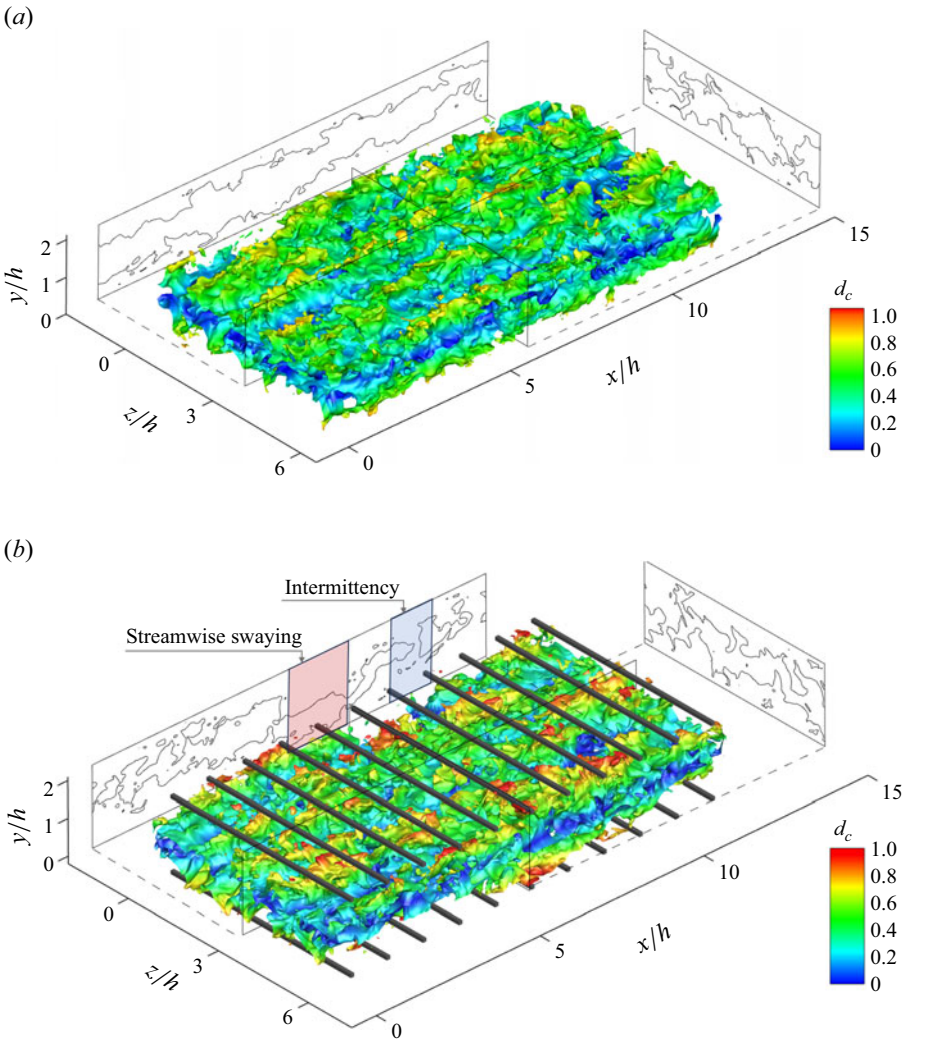


Figure 11. Instantaneous isosurface of the QC, defined by the threshold $u/U_{CL} = 0.95$, for (*a*) the SM case and (*b*) the P12 case. The isosurface is coloured by the distance d_c from the channel centreline. The locations of the roughness elements in (*b*) are indicated by the black bars. Contours of the instantaneous streamwise velocity are also shown on the x–y plane at $z/h = 3$, and the y–z plane at $x/h = 6$.

indicate sweeps. In the rough case P12 (figure 11*b*), the streamwise coherence of the isosurface is markedly disrupted. Compared with the SM case, the y–z section shows that the QC boundary becomes more fragmented in the spanwise direction, and in the streamwise direction, the QC boundary exhibits abrupt alternation of thick and thin segments consistent with spanwise blockage and element-scale separation/reattachment with wakes in and above the bar array. It is precisely this mechanism that leads to more intense streamwise swaying of the QC relative to the smooth-wall case. From the isosurface visualisation, more QC structures on the rough wall extend closer to the wall, while more regions are lifted towards the channel centreline under the influence of low-speed structures from the rough surface.

https://doi.org/10.1017/jfm.2026.11950 Published online by Cambridge University Press

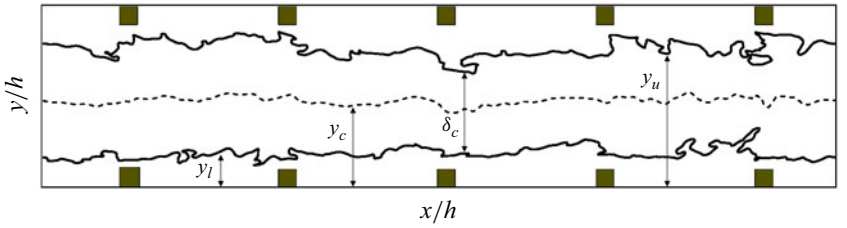


Figure 12. Schematic of QC geometry definitions on an x–y slice. Solid curves denote the instantaneous QC boundaries; the local thickness is $\delta_c = y_u - y_l$, and the centre position $y_c = (y_u + y_l)/2$ is shown by the dashed curve.

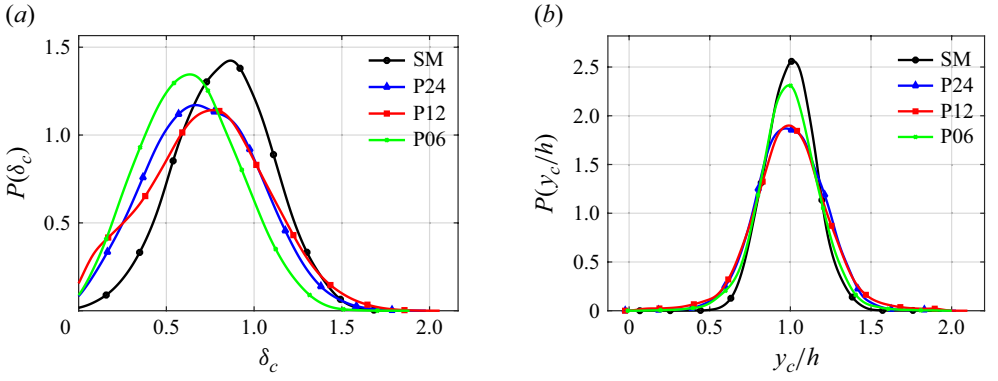


Figure 13. The PDFs of (*a*) the core thickness δ_c, and (*b*) the core centre position y_c/h, for the smooth-wall (SM) and rough-wall (P06, P12, P24) cases.

The QC boundaries are identified on x–y slices at fixed z/h, using the threshold $U/U_{CL} = 0.95$, and after a de-bubbling/post-processing step to remove internal voids and small disconnected regions inside the enclosed contours to enforce boundary continuity, locating the upper and lower boundary coordinates $y_u(x, z)$ and $y_l(x, z)$ at each streamwise position as illustrated in figure 12. The local QC thickness and centre position are then defined as

$$\delta_c(x, z) = y_u(x, z) - y_l(x, z), \quad y_c(x, z) = \frac{y_u(x, z) + y_l(x, z)}{2}. \tag{5.1}$$

With the slice-based boundary identification established, figure 13(*a*) and table 3 show that roughness reduces the mean QC thickness, and increases its spread relative to the smooth wall. For the SM case, the PDF of δ_c exhibits a near-Gaussian distribution, with $\mu/h = 0.79$ and $\sigma/h = 0.27$ (Kwon *et al.* 2014). For the rough-wall cases, the mean decreases non-monotonically across P06, P12 and P24, while the standard deviation rises as shown in table 3. Here, P12 has a larger mean thickness than P24 ($\mu/h = 0.73$ versus $\mu/h = 0.71$), despite its smaller pitch – a counterintuitive result given that P24's larger roughness spacing would be expected to provide more available space for the QC to expand. This indicates that P12 features more QC regions extending towards the wall, and implies more frequent momentum transfer processes between the QC and the non-core regions. The increased variance indicates more frequent and larger departures of δ_c from its mean. Instantaneous snapshots highlight the same tendency: sweep/ejection

https://doi.org/10.1017/jfm.2026.11950 Published online by Cambridge University Press

Case	δ_c/h		y_c/h		$\gamma\ (y/h=1)$
	μ/h	σ/h	μ/h	σ/h	
P24	0.71	0.31	1.00	0.21	0.26
P12	0.73	0.34	1.00	0.23	0.31
P06	0.63	0.28	0.99	0.19	0.26
SM	0.79	0.27	1.00	0.16	0.08
P24H	0.70	0.31	1.00	0.20	0.26

Table 3. Summary of key statistics for the core thickness (δ_c) and centre position (y_c), alongside the intermittency factor (γ) at the channel centreline, for all cases. The mean (μ) and standard deviation (σ) are calculated from the respective PDFs.

events (figure 10) and large-magnitude d_c patches on the QC isosurface (figure 11) reflect enhanced thickening–thinning intermittency. The PDFs also retain finite density at $\delta_c = 0$, indicating local core breakage where the core vanishes locally, which is associated with large-scale, low-speed structures in the outer region (figure 11).

The wall-normal centre position of the QC, y_c, quantifies the meandering motion of the QC (figure 13(*b*), table 3). The mean y_c remains near the centreline for all cases, whereas the standard deviation increases notably in the rough-wall flows, from 0.16 (SM) to 0.19 (P06), 0.23 (P12) and 0.21 (P24), indicating stronger meandering in the presence of a rough wall. For P06, the smaller increase is consistent with short-pitch bars, where separation behind successive elements forms a strong-shear mixing layer that continues to develop at small spacing, producing an effectively planar interface to the outer flow (Chung *et al.* 2021). Case P12 exhibits stronger meandering than P24 even with its smaller pitch; combined with its larger mean δ_c, this points to more frequent approach of the QC boundary towards the wall in P12.

To further quantify the spatial distribution of the QC, the intermittency profile $\gamma(y)$ is defined as the fraction of time for which the flow resides outside the QC at different wall-normal locations y/h (Kwon *et al.* 2014). Figure 14 presents $\gamma(y)$ for all cases. At the channel centreline ($y/h = 1$), the smooth wall yields $\gamma \approx 0.08$, whereas the core excludes the centreline much more frequently in the rough-wall cases, arising from both intensified core meandering and roughness-induced core breakage. For P06, the increase in γ is most pronounced within $0.05 \leq y/h \leq 0.75$, consistent with QC compression inferred from its smaller mean δ_c. For P12, γ is lower than the smooth-wall profile over a substantial near-wall range ($y/h < 0.5$), indicating higher QC occupancy near the wall. Towards the centreline, γ increases and reaches the largest value among rough cases. Relative to other configurations, P12 therefore combines more frequent near-wall QC presence, with stronger centreline intermittency consistent with its larger variances of y_c and δ_c reported in table 3. The sensitivity of these QC geometry statistics to Reynolds number and to streamwise domain length is assessed in Appendix C through comparisons with cases P24H ($Re_\tau = 590$) and P24L ($L_x = 24h$), respectively.

Figure 15 illustrates the topological difference of the QC related to the out-of-core turbulent motions of the QC based on the above observations of the QC thickness, centre position and intermittency. Case P24 displays the typical rough-wall response (figure 15*a*) in which the core is notably thinner in all rough-wall cases compared with the SM case, and the thickness fluctuations are broader and the centre position variability is higher, and the centreline is interrupted more often. Case P12 exhibits the strongest wall-normal organisation among the rough cases (figure 15*b*). Both δ_c and y_c fluctuate more than in the other configurations, and the mean thickness is larger than in P24 despite

https://doi.org/10.1017/jfm.2026.11950 Published online by Cambridge University Press

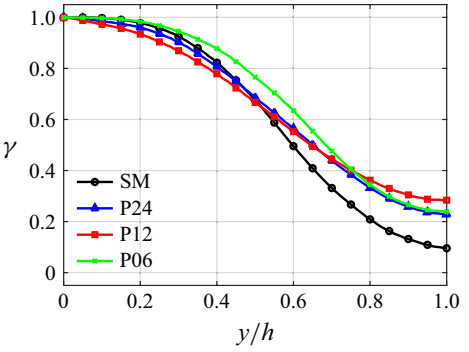


Figure 14. Profiles of the intermittency factor γ as a function of the wall-normal position y/h, for the smooth-wall (SM) and rough-wall (P06, P12, P24) cases.

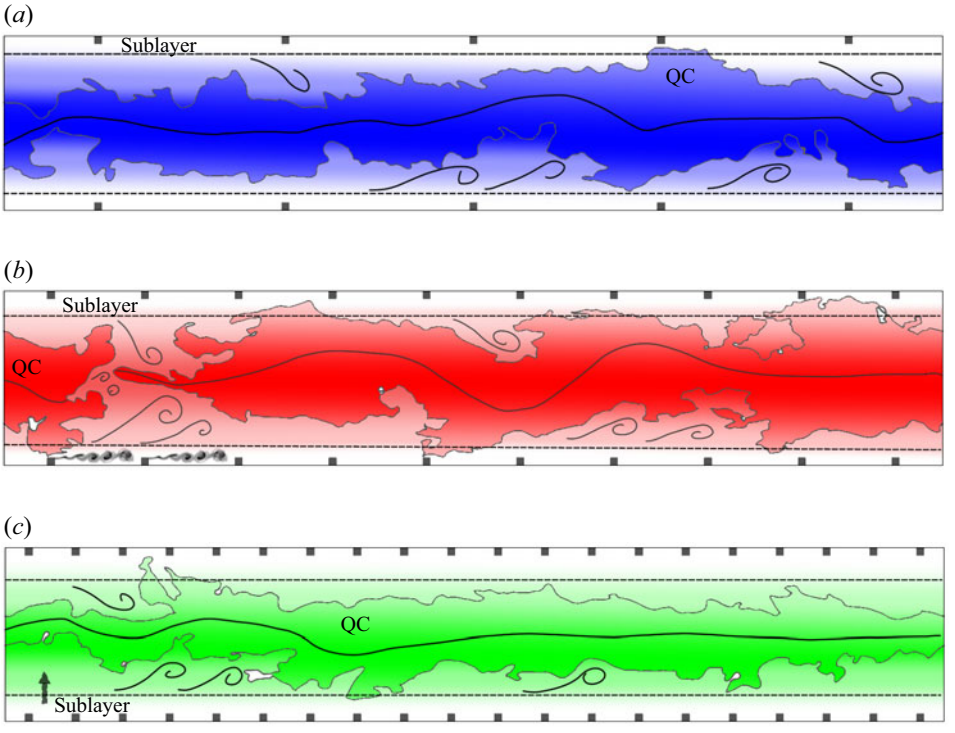


Figure 15. Schematic of the quiescent-core boundary for roughness configurations on an x–y slice: (*a*) P24, (*b*) P12, (*c*) P06.

the smaller pitch. The intermittency profile combines frequent near-wall QC occupancy, evidenced by γ falling below the smooth-wall curve over a substantial near-wall range, with the highest interruption rate at the centreline. Altogether, P12 shows a pronounced meandering in which bulk excursions deepen the near-wall reach of the high-speed core while vacating the centre more frequently. Case P06 remains closest to the smooth wall in variability (figure 15*c*). The QC is the thinnest on average among all cases, its centre position fluctuations are moderate, and the increase in intermittency is concentrated at

https://doi.org/10.1017/jfm.2026.11950 Published online by Cambridge University Press

intermediate heights, consistent with a short-pitch configuration where a developing inter-element mixing layer yields a quasi-planar imprint on the outer flow. The intensified meandering and thinning behaviours of the QC are linked to interfacial flow characteristics and momentum transfer from the wall up to the core boundary, investigated in the next section.

6. Statistical characteristics of the QC boundary and exterior

The latter part of the study examines how roughness affects the outer-layer structural organisation and momentum transport from the wall into the core. As observed in § 5, roughness modifies the topological characteristics of the QC, including its thickness, meandering and intermittency with trends that depend on the roughness density. The present section conducts interfacial conditional-averaged analyses to reveal the momentum transfer across the QC boundary.

6.1. *Interfacial dynamics of the QC boundary*

For wall-normal conditional averaging of in-core and out-of-core profiles, zonal mean statistics are employed. At a given wall-normal position y, the conditional mean streamwise velocities are designated as $\tilde{u}$ (for locations inside the QC) and $\hat{u}$ (for locations outside the core), corresponding to the zonal averages within and outside the core, respectively. The overall mean streamwise velocity U is derived as a weighted combination of $\tilde{u}$ and $\hat{u}$, with the weights determined by the intermittency factor γ:

$$U = \gamma\hat{u} + (1-\gamma)\tilde{u} \tag{6.1}$$

Additionally, the zonal streamwise turbulent intensity profiles are defined to quantify fluctuations within each zone:

$$\tilde{u}'^2 = \widetilde{(u-\tilde{u})^2}, \quad \hat{u}'^2 = \widehat{(u-\hat{u})^2}, \tag{6.2}$$

where u denotes the instantaneous streamwise velocity, and U represents the unconditional mean streamwise velocity across the entire flow field.

Figure 16 shows the conditional means of the streamwise velocity and its fluctuation intensities. Across all cases, the in-core mean $\tilde{u}$ is nearly uniform and close to U_{CL}, indicating that the QC remains a high-speed, low-shear zone even with rough walls. The near-wall, out-of-core mean velocity profile $\hat{u}$ follows the global mean profile of U and is governed by the roughness sublayer, and typically a smaller pitch (e.g. P06) yields a lower near-wall $\hat{u}$. Approaching the centreline, $\hat{u}$ values from different rough-wall cases tend to converge. For P12, away from the centreline, $\tilde{u}$ exceeds that of the other rough cases, suggesting more frequent downwash of high-speed fluid from the QC towards the wall under stronger meandering, whereas near the centreline, $\hat{u}$ is the smallest among the rough cases, indicating that the QC more often vacates the centreline, and the exterior flow is less accelerated.

The in- and out-of-core conditionally averaged streamwise turbulent intensities in figure 16 show that the QC interior flow has a comparatively low disturbance level, with fluctuations concentrated at the tortuous QC boundary. Near the centreline, $\hat{u}'^2$ falls below $\tilde{u}'^2$, in line with Kwon *et al.* (2014), indicating that out-of-core structures reaching the centreline have relatively mild turbulent levels. Over rough walls, the near-wall $\hat{u}'^2$ is enhanced by the roughness sublayer, whereas at the centreline, $\hat{u}'^2$ is similar across cases. In this context, P12 exhibits larger $\tilde{u}'^2$ inside the core, indicating stronger in-core

https://doi.org/10.1017/jfm.2026.11950 Published online by Cambridge University Press

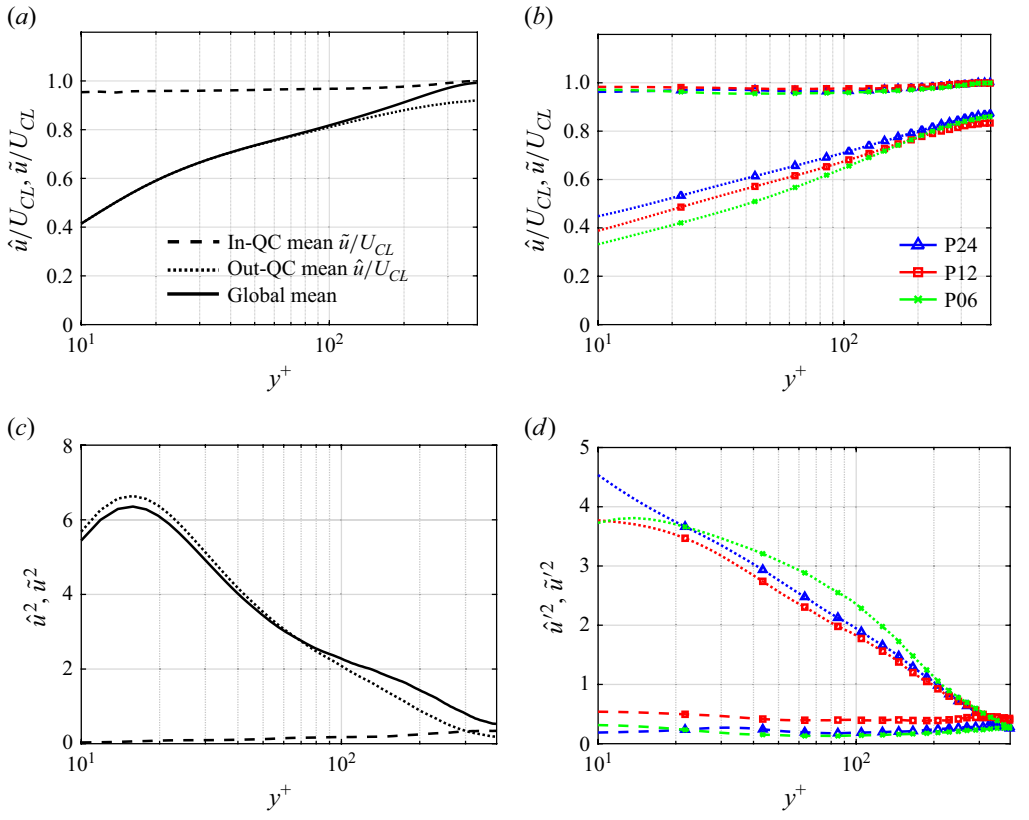


Figure 16. Conditional statistics of mean velocity and turbulence intensity profiles: (*a*,*c*) smooth-wall cases, (*b*,*d*) rough-wall cases, for (*a*,*b*) streamwise mean velocity profiles U, $\tilde{u}$, $\hat{u}$, (*c*,*d*) streamwise turbulent intensity profiles $\overline{u'^2}$, $\tilde{u}'^2$, $\hat{u}'^2$. For all plots, dashed lines correspond to the conditional average inside the core $\tilde{(\cdot)}$ and dotted lines correspond to the conditional average outside the core $\hat{(\cdot)}$. In (*a*,*c*), solid lines denote the unconditional (global) mean $\bar{(\cdot)}$.

streamwise fluctuations associated with the swaying mode. For P06, the near-wall $\hat{u}'^2$ is comparatively higher, reflecting the more direct influence of the roughness sublayer.

Figure 17 shows the interfacial averages in an interface-relative coordinate. Let y_I denotes the instantaneous boundary height (y_u or y_l), and define

$$\xi = y - y_I, \quad \xi > 0 \text{ points into the QC}, \tag{6.3}$$

with interfacial averaging along the instantaneous boundary:

$$\langle q \mid \xi \rangle_\Sigma = \frac{1}{\mathcal{L}_\Sigma} \int_\Sigma q(y_I + \xi)\, \mathrm{d}s, \tag{6.4}$$

where Σ is the boundary curve in the x–z plane, ds is the line element, and $\mathcal{L}_\Sigma$ is its arc length. Here, q denotes any flow quantity of interest (e.g. u, Ω_z or Reynolds shear stress $u'v'$). Equation (6.4) defines the interfacial average of q evaluated at a fixed normal distance ξ from the instantaneous QC boundary y_I, integrated along the boundary Σ, and normalised by the boundary length $\mathcal{L}_\Sigma$. This operation aligns profiles from different realisations to a common interface-relative origin ($\xi = 0$), so that sharp gradients across the boundary are not smeared by the meandering nature of the interface. The spanwise

https://doi.org/10.1017/jfm.2026.11950 Published online by Cambridge University Press

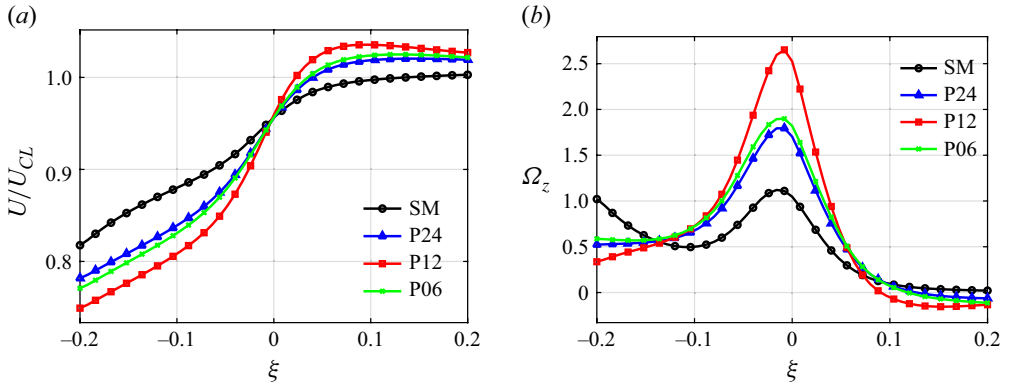


Figure 17. Conditionally averaged profiles across the core boundary ($\xi = 0$): (a) streamwise velocity U/U_{CL}, and (b) spanwise vorticity Ω_z, plotted as functions of the interface-relative coordinate ξ. Profiles are shown for the smooth-wall (SM) and rough-wall (P24, P12, P06) cases.

vorticity is

$$\Omega_z = \frac{\partial v}{\partial x} - \frac{\partial u}{\partial y}. \tag{6.5}$$

The velocity profiles in figure 17(a) display a sharp jump at $\xi = 0$, accompanied by a peak of Ω_z, which together mark a narrow region of concentrated shear that has been observed in the smooth-wall flows (Kwon *et al.* 2014; Chen *et al.* 2020). All rough-wall cases show larger velocity jumps and stronger vorticity peaks across the QC boundary around $\xi \approx 0$. This may be attributed to the roughness sublayer lowering $\hat{u}$ immediately outside the boundary, while a thinner QC places the boundary at an interior location with higher speed, which contributes to the observed increase in the velocity difference. Among the rough-wall cases, P12 exhibits the largest velocity jump and the strongest vorticity. This could be linked to the stronger meandering, which more frequently brings the QC boundary close to the wall.

6.2. *Momentum transfer on the QC boundary and its exterior*

Linear stochastic estimation (LSE) (Adrian 1996; Zhou *et al.* 1999) is used to relate quadrant events to 3-D coherent structures at a near-wall height ($y^+ \approx 47$) and on the QC boundary. The LSE method aims to obtain the best linear approximation of the conditional average of the fluctuating velocity field at any spatial position x', given a predefined velocity event vector at a specified location x. The best linear estimate of the 3-D fluctuating velocity field $\check{u}_i'(x')$ is expressed as

$$\check{u}_i'(x') = \sum_{j=1}^{3} L_{ij}(x', x) \times u_j^*(x), \tag{6.6}$$

where $L_{ij}(x', x)$ denotes the linear estimation coefficient matrix. Here, $u_j^*(x)$ is the velocity event vector at x, chosen as the second-quadrant (Q2) ejection event. To minimise the mean square error between the linear estimate $\check{u}_i'(x')$ and the conditional average $\langle u_i'(x') \mid u_j^*(x) \rangle$, the coefficients $L_{ij}(x', x)$ are solved via the Yule–Walker equation:

https://doi.org/10.1017/jfm.2026.11950 Published online by Cambridge University Press

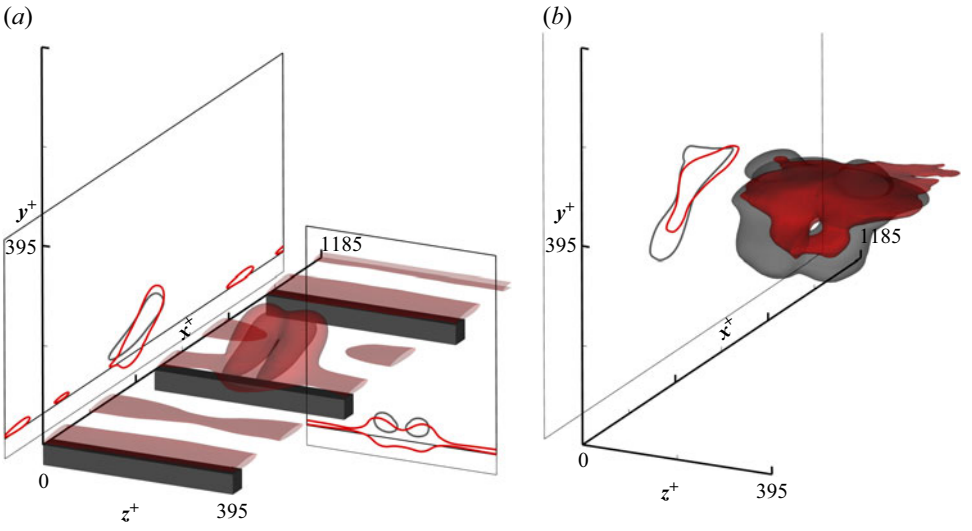


Figure 18. Three-dimensional schematic of the LSE-conditioned Q2 structure (*a*) at $y^+ \approx 47$ and (*b*) on the instantaneous QC boundary for the smooth wall (grey) and the P12 rough wall (red). Semi-transparent isosurfaces depict the conditional structures, and thin contours show intersections with orthogonal x–y and y–z planes. Spanwise-aligned rectangular blocks indicate the roughness elements.

$$\sum_{j=1}^{3} \langle u_k^*(x)\, u_j^*(x)\rangle\, L_{ij}(x', x) = \langle u_i'(x')\, u_k^*(x)\rangle. \tag{6.7}$$

Here, $\langle\cdot\rangle$ represents the global ensemble average. The term $\langle u_k^*(x)\, u_j^*(x)\rangle$ is the autocorrelation of the event vector components, and $\langle u_i'(x')\, u_k^*(x)\rangle$ is the cross-correlation between the fluctuating velocity field and the event vector. The total velocity field, combining the mean velocity and the LSE fluctuating velocity, is given by the best linear estimate of the total flow field:

$$u_{i,LSE}(x') = U_i + \breve{u}_i'(x'). \tag{6.8}$$

Vortices in the reconstructed fields are visualised using the swirling strength criterion λ_{ci} (Zhou *et al.* 1999; Christensen & Adrian 2001). The swirling strength is defined as the imaginary part of the complex eigenvalue pair of the local velocity gradient tensor ∇u. A vortex core is identified, where ∇u possesses a pair of complex conjugate eigenvalues, and λ_{ci} is taken as the magnitude of their imaginary part. Regions where $\lambda_{ci} > 0$ indicate local swirling motion. The squared swirling strength λ_{ci}^2 is used as the isosurface variable, following the convention of Christensen & Adrian (2001). The conditioning event is taken in the Q2 quadrant at the red cross location in figure 20 below, identified from the covariance integrand $u'v'\,P(u', v')$. To enable consistent cross-case comparisons, isosurfaces are rendered at a fixed percentage of the per-case maximum λ_{ci}^2 rather than at a uniform absolute threshold. Values of 5 % of the case maximum are used for the fixed-height conditioning cases, and 2 % for the QC-boundary conditioning cases, with the resulting structural extents L_x^+ and L_y^+ summarised in table 4.

Figure 18(*a*) shows, in three dimensions, that for P12, the upstream legs of the hairpin structure extend into the gaps between roughness elements, consistent with periodic wakes that form behind each element and interact with the hairpin structure. The hairpin head rises further from the wall, increasing the wall-normal extent of the structure. In x–y

https://doi.org/10.1017/jfm.2026.11950 Published online by Cambridge University Press

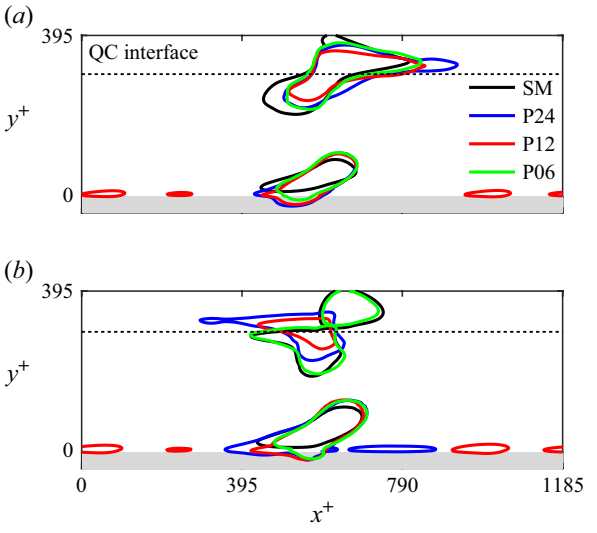


Figure 19. The LSE-conditioned structures in 2-D x–y planes at $z^+ = 157.5$ for smooth and rough walls. (*a*) The Q2 sections at $y^+ \approx 47$ and on the instantaneous QC boundary for SM and the rough-wall configurations P06, P12 and P24. (*b*) The Q4 sections at $y^+ \approx 47$ and on the instantaneous QC boundary for the same set of cases. The shaded region indicates the roughness height range $0 \leq y^+ \leq k^+$.

planes at $y^+ \approx 47$, $z^+ = 157.5$ shown in figure 19(*a*), the upper extent of the Q2 structure is comparable across the rough-wall cases, while the streamwise extent and the wall-normal penetration vary with pitch, as quantified in table 4. Among them, P24 displays the longest upstream-leg extension ($L_x^+ \approx 250$) and the deepest penetration into the cavities, enabled by the larger element spacing that accommodates more persistent wakes, while P06 yields the most compact footprint ($L_x^+ \approx 199$). The modulation of Q4 at this height is stronger than that of Q2, with a longer upstream tail, and a clearer wall-normal penetration between elements as p/k increases (figure 19*b*), with P24 exhibiting the largest streamwise extent ($L_x^+ \approx 350$). These patterns indicate that near-wall momentum transfer is sensitive to the element spacing.

The Q2-conditioned vortical structure at the QC boundary is compared for SM and P12 in figure 18(*b*). Within the QC interior, the structure is predominantly streamwise-elongated with limited wall-normal penetration, reflecting the quiescent, high-speed character of the core. On the exterior side, a pair of inclined counter-rotating quasi-streamwise vortex legs is present, consistent with the organisation of ejection events in smooth-wall flows (Zhou *et al.* 1999; Christensen & Adrian 2001). The spatial extent of these legs is appreciably larger for the smooth wall, indicating that the ejection-associated structure is more spatially confined in the rough-wall case.

The x–y cross-sections in figure 19 further quantify these differences. For the Q2 event at the QC boundary (figure 19*a*), all rough-wall cases exhibit a reduced wall-normal extent relative to SM, with P12 showing the most pronounced reduction, while P24 retains a comparatively extended streamwise reach. For the Q4 event (figure 19*b*), P06 most closely approaches the smooth-wall reference in both L_x^+ and L_y^+, whereas P12 yields the most compact structure in both metrics, consistent with its most disrupted QC geometry among the rough cases.

Figure 20 presents the covariance integrand $u'v'\,P(u', v')$ sampled along the instantaneous QC boundary. The red cross marks the conditioning event identified from

https://doi.org/10.1017/jfm.2026.11950 Published online by Cambridge University Press

Condition		SM	P24	P12	P06
Q2, $y^+ \approx 47$	$\lvert E\rvert$	9.5	9.3	7.6	9.1
	P_0	0.025	0.020	0.026	0.028
	L_x^+	234.5	250.4	232.0	199.1
	L_y^+	78.7	130.1	124.0	115.9
Q4, $y^+ \approx 47$	$\lvert E\rvert$	6.6	7.6	6.6	7.3
	P_0	0.057	0.038	0.046	0.045
	L_x^+	258.0	349.9	277.2	228.6
	L_y^+	99.0	146.5	146.6	143.5
Q2, QC boundary	$\lvert E\rvert$	3.7	2.9	2.9	2.7
	P_0	0.169	0.375	0.268	0.338
	L_x^+	359.2	427.7	335.8	330.1
	L_y^+	195.2	153.9	122.0	163.3
Q4, QC boundary	$\lvert E\rvert$	5.5	6.4	5.5	5.3
	P_0	0.065	0.058	0.060	0.072
	L_x^+	326.0	355.5	189.3	315.7
	L_y^+	213.1	118.8	75.3	204.2

Table 4. The LSE conditioning parameters and reconstructed-structure metrics. Here, $|E| = \alpha(u^{*2} + v^{*2})^{1/2}$ is the event-vector amplitude (wall units, $\alpha = 3$), P_0 is the probability density at the conditioning point, obtained by bilinear interpolation of the joint PDF, and L_x^+ and L_y^+ are streamwise and wall-normal extents of the primary λ_{ci}^2 isosurface contour extracted at $z^+ = 157.5$, using a threshold 5 % of the case-maximum λ_{ci}^2 for the fixed-height cases, and 2 % for the QC-boundary cases.

the joint PDF, whose amplitude $|E|$ and probability density P_0 are reported in table 4. The distributions exhibit a general asymmetry: the positive-u' side extends to larger amplitudes than the negative-u' side, consistent with the systematically larger $|E|$ for Q4 than for Q2 across all cases. For the Q2 contributions, the smooth-wall distribution is the most extended in the streamwise direction, whereas the rough-wall cases are contracted in $|u'|$ but enhanced in wall-normal amplitude v', most markedly for P12. The low P_0 for P12 reflects a broad redistribution of events towards larger amplitudes, rather than a concentration at the most probable velocity. For the Q4 contributions, the rough-wall distributions are displaced towards larger amplitudes of both $|u'|$ and $|v'|$ relative to SM, with P12 exhibiting the strongest bias toward elevated v', and P06 remaining closest to the smooth-wall reference. This case ordering is consistent with the ranking of interfacial velocity jumps in figure 17(*a*).

The wall-normal evolution of quadrant fractions complements these observations. The fractional contributions $\langle u'v'\rangle_Q/\langle u'v'\rangle$ versus y^+ in figure 21 show that P24 and P06 approximately follow the smooth-wall reference, with modest increases of Q2 and Q4 in the QC exterior. Case P12 departs for $y^+ \gtrsim 200$, and all four quadrant contributions separate from the smooth-wall curves. This indicates that near the QC boundary, stronger interfacial shear modifies the composition of momentum-carrying events, echoing the roughness-sensitive Q2 behaviour noted by Zhang *et al.* (2026) in boundary layers.

Strong-event weighting is assessed using the hyperbolic-hole filter following Lu & Willmarth (1973). For quadrant Q at fixed y,

https://doi.org/10.1017/jfm.2026.11950 Published online by Cambridge University Press

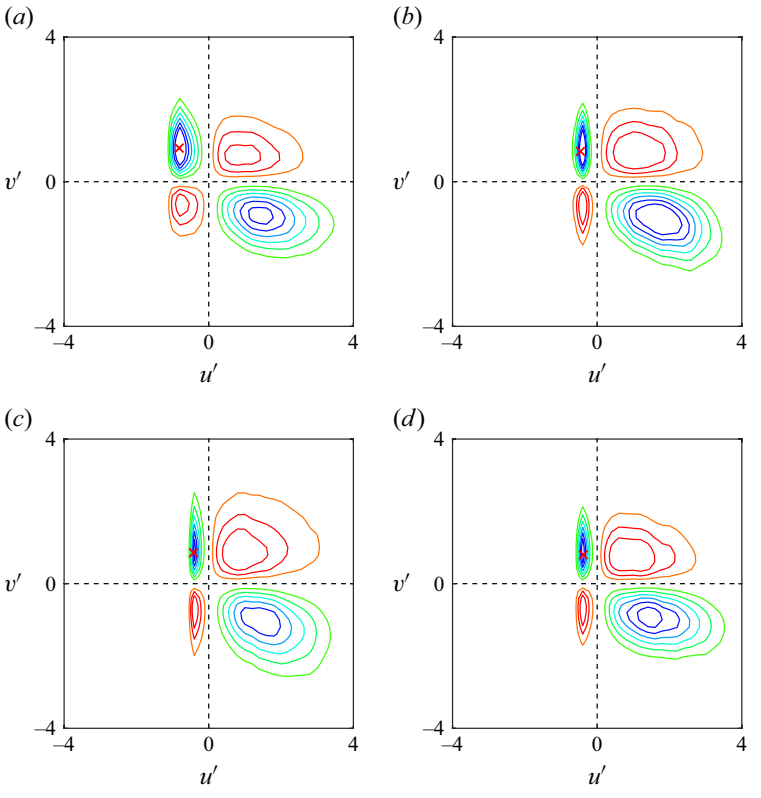


Figure 20. Contours of the covariance integrand $u'v'\,P(u', v')$ on the instantaneous QC boundary. Contour levels are shown with an increment $\Delta = 0.01$ for negative values in the range $[-0.08, -0.02]$ and for positive values in the range $[0.01, 0.03]$. Plots show the covariance integrand for (*a*) SM, (*b*) P24, (*c*) P12, and (*d*) P06.

$$\frac{\langle u'v'\rangle_Q(H)}{\langle u'v'\rangle} = \frac{\iint_{(u',v')\in Q} u'v'\,P(u', v' \mid y)\,I(H)\,\mathrm{d}u'\,\mathrm{d}v'}{\langle u'v'\rangle}, \tag{6.9}$$

$$I(H) = \big(|u'v'| > H\,\langle -u'v'\rangle\big). \tag{6.10}$$

The hyperbolic-hole analysis at the instantaneous QC boundary (figure 22) shows that the dominant stress-carrying events are concentrated in Q1 and Q4, with Q2 contributing only a minor fraction of the total stress. This is consistent with the rightward bias of the covariance integrand in figure 20, reflecting the character of the QC boundary as a high-speed interface across which fast fluid impinges upon the slower exterior. Among the cases, the smooth-wall Q2 contribution shifts towards larger H relative to all rough-wall cases, indicating that ejection stress is more concentrated in strong events for the smooth wall, whereas rough-wall ejections are comparatively diffuse. The case ordering of Q4 contributions follows the amplitude redistribution pattern in figure 20: P12 exhibits the largest Q4 contribution across the full range of H, and P06 remains closest to the smooth-wall reference.

Quadrant fractions across the interface-relative coordinate ξ (negative outside the core, and positive inside) in figure 23 highlight where roughness effects are concentrated. Stresses vary sharply on the exterior side, and become nearly case-independent inside the QC. Immediately outside the interface ($\xi \approx -0.1$), P12 exhibits the largest magnitudes

https://doi.org/10.1017/jfm.2026.11950 Published online by Cambridge University Press

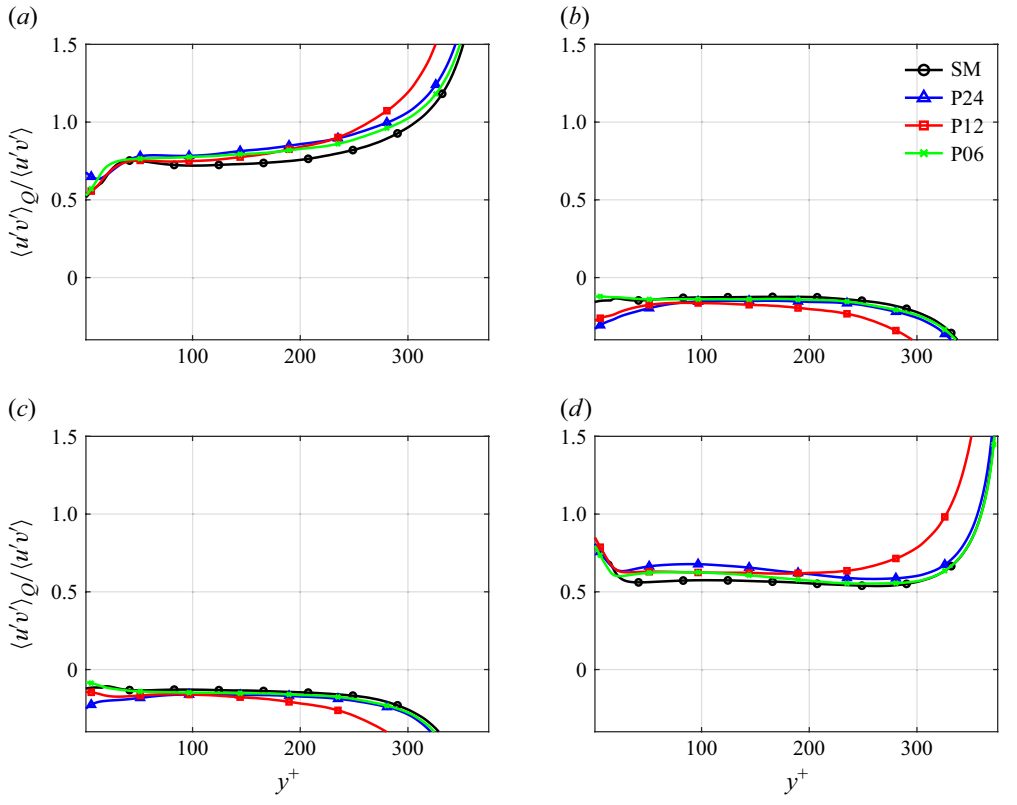


Figure 21. Fractional quadrant contributions to the Reynolds shear stress plotted versus the wall coordinate y^+. The ordinate is $\langle u'v'\rangle_Q/\langle u'v'\rangle$, with $\langle u'v'\rangle_Q = \iint_{(u',v')\in Q} u'v'\, P(u', v' \mid y)\, \mathrm{d}u'\, \mathrm{d}v'$. Plots are arranged by quadrant: (*a*) Q2, (*b*) Q1, (*c*) Q3, (*d*) Q4. Curves correspond to SM and the rough-wall configurations P24, P12 and P06.

across all quadrants, which indicates that all types of events are intensified at the boundary for this case. This is consistent with the larger velocity jump and the stronger spanwise vorticity peak observed for P12 in figure 17(*a*). For P06, increases in quadrant contributions occur slightly farther from the interface on the exterior side ($\xi \approx -0.2$), which aligns with the influence of the roughness sublayer – its elevation promotes momentum exchange that extends towards the QC boundary.

The interfacial stresses discussed above form part of the total stress balance. To establish how each stress component contributes to the momentum transport across roughness configurations, figure 24 presents the double-averaged decomposition

$$\tau^+_{total} = \tau^+_\nu + \tau^+_R + \tau^+_D, \tag{6.11}$$

where $\tau^+_\nu = (\nu\, \mathrm{d}U/\mathrm{d}y)/u^2_\tau$ is the viscous stress, $\tau^+_R = -\langle\overline{u'v'}\rangle/u^2_\tau$ is the Reynolds shear stress, and $\tau^+_D = -\langle\overline{u}''\,\overline{v}''\rangle/u^2_\tau$ is the dispersive shear stress, with $\overline{u}'' = \overline{u} - U$ and $\overline{v}'' = \overline{v} - V$ denoting the departures of the time-averaged velocities from their spatial averages. The three terms represent, respectively, the contributions of viscous friction, turbulent fluctuations and time-averaged spatial flow inhomogeneity to the total momentum transport over rough walls.

https://doi.org/10.1017/jfm.2026.11950 Published online by Cambridge University Press

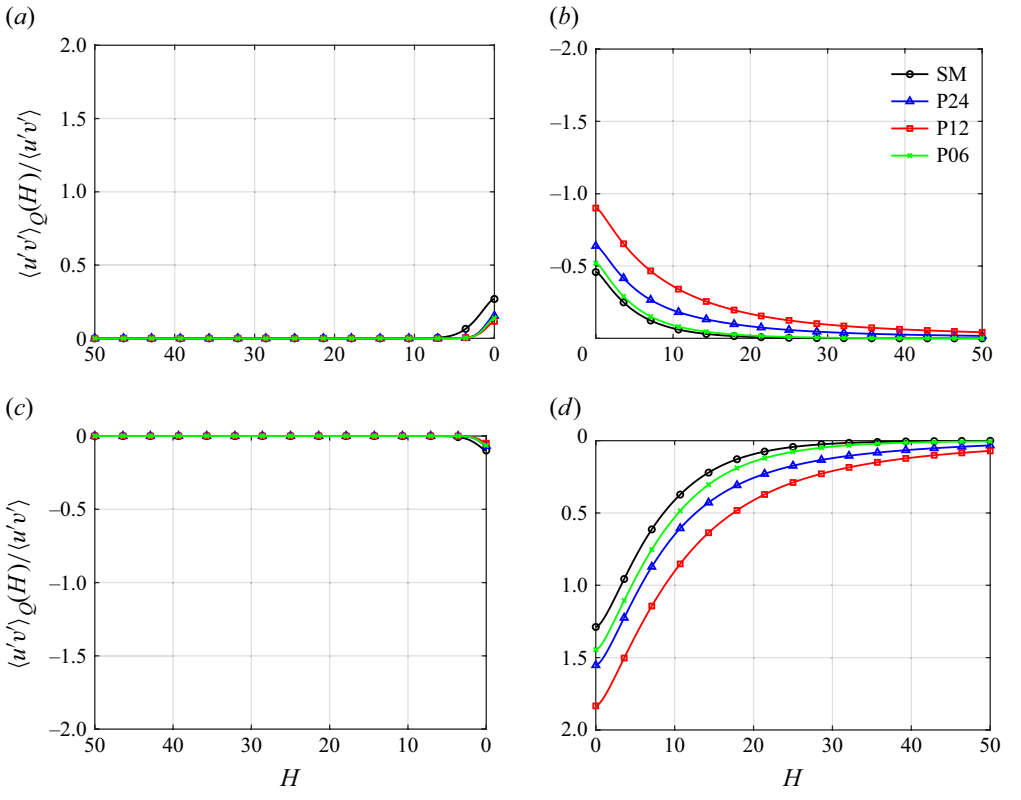


Figure 22. Hyperbolic-hole filtered quadrant contributions on the instantaneous QC boundary. The ordinate is $\langle u'v'\rangle_Q(H)/\langle u'v'\rangle$, with the indicator $I(H) = (|u'v'| > H\,\langle -u'v'\rangle)$. Plots are for (*a*) Q2, (*b*) Q1, (*c*) Q3, (*d*) Q4. For display purposes, the abscissa is reversed for Q2 and Q3, and the ordinate sign is reversed for Q1 and Q4. Curves correspond to SM, P24, P12 and P06.

For the rough-wall cases, τ_v^+ exhibits a positive peak near the roughness crest, and decays rapidly above it, with the peak width narrowing as p/k decreases, while its direct contribution to the outer-layer momentum balance remains limited.

The profile of τ_D^+ differs markedly among the three rough-wall cases. For P06 (figure 24*d*), τ_D^+ attains a small negative value near the crest height, and decays rapidly above it, remaining the smallest in magnitude among the rough-wall cases across the full wall-normal extent. The distributions of both τ_D^+ and τ_R^+ remain the closest to the smooth-wall reference among the rough-wall cases, consistent with the near-smooth-wall QC geometry and interfacial statistics established in § 5–§ 6.1.

For P12 (figure 24*c*), the negative peak of τ_D^+ near the crest height is the largest in absolute value among all three rough-wall cases, indicating that the spatially non-uniform time-averaged flow transports a greater fraction of momentum upwards against the mean gradient in this configuration. The elevated outer-layer τ_R^+ reflects the intensified wall-normal turbulent motions and enhanced interfacial shear documented in § 5–§ 6.1, both of which are associated with the pronounced wall-ward QC excursions of P12.

For P24 (figure 24*b*), the negative region of τ_D^+ is broader in wall-normal extent, and its influence persists further into the outer layer relative to the other cases. The larger element spacing allows the time-averaged recirculation within each cavity to develop more fully, sustaining a spatially heterogeneous mean flow pattern over a greater wall-normal distance.

https://doi.org/10.1017/jfm.2026.11950 Published online by Cambridge University Press

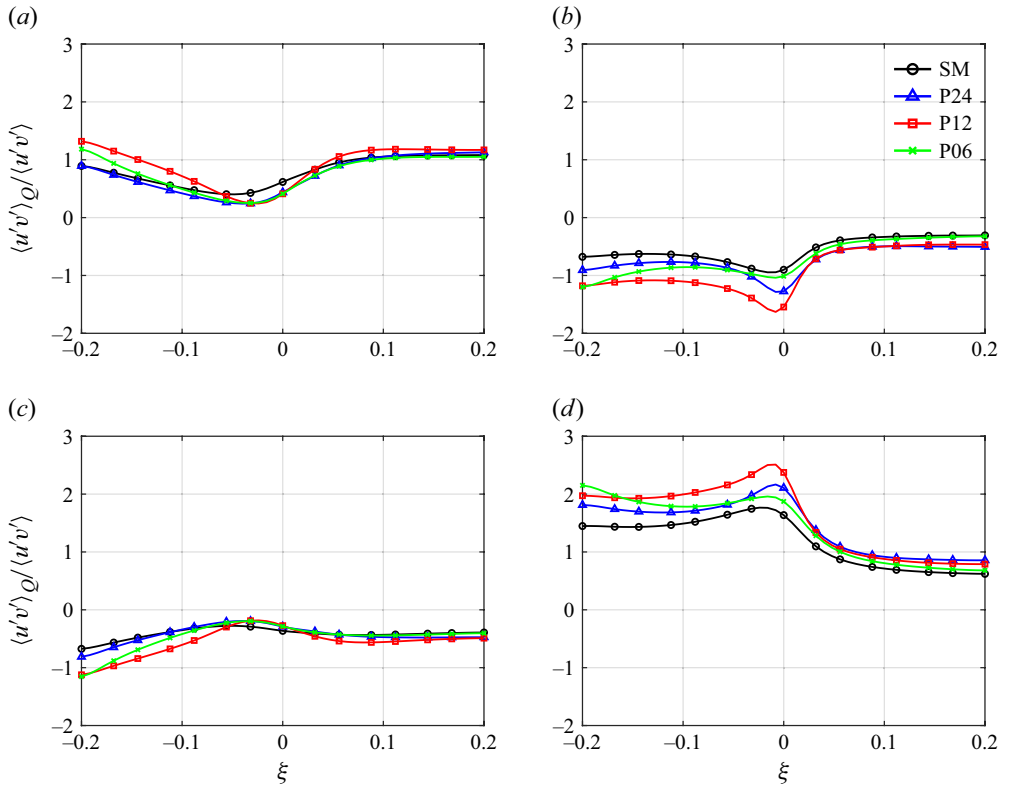


Figure 23. Quadrant-conditioned fraction of the Reynolds shear stress across the QC interface, plotted against the interface-relative coordinate ξ (positive into the core, and $\xi = 0$ at the instantaneous interface, as in figure 15). The ordinate is $\langle u'v'\rangle_Q/\langle u'v'\rangle$. Plots are for (*a*) Q2, (*b*) Q1, (*c*) Q3, (*d*) Q4. Curves correspond to SM, P24, P12 and P06.

Overall, under a strong swaying mode, P12 shows the expected signature at the QC boundary: stronger interfacial shear leads to larger deviations from the mean and therefore to stronger events. Case P06 remains close to the smooth-wall behaviour in both structure and statistics, in line with its QC geometry. Taken together, the covariance integrand, the conditional structures and the quadrant analyses suggest that similarity in QC geometry is linked to similarity in momentum transfer. For the present configuration, momentum transfer near the wall appears to be primarily influenced by the roughness sublayer, while further away from the wall, its behaviour is more aligned with the evolution of the meandering QC.

7. Conclusions

This study compares the quiescent core (QC) over rough surfaces with that over smooth surfaces, and uses the changes in the geometric characteristics of the QC to describe the influence of the distribution of spanwise-uniform roughness bars on the channel centre, i.e. the main momentum-containing region. Based on the identification results of the KDE-based velocity–PDF method, a unified QC boundary at $U/U_{CL} \approx 0.95$ is adopted owing to the consistent modal velocity of the QC across both rough- and smooth-surface configurations. On this basis, the geometric characteristics of the identified QCs on rough and smooth surfaces, including the thickness δ_c, centre position y_c, and intermittency γ,

https://doi.org/10.1017/jfm.2026.11950 Published online by Cambridge University Press

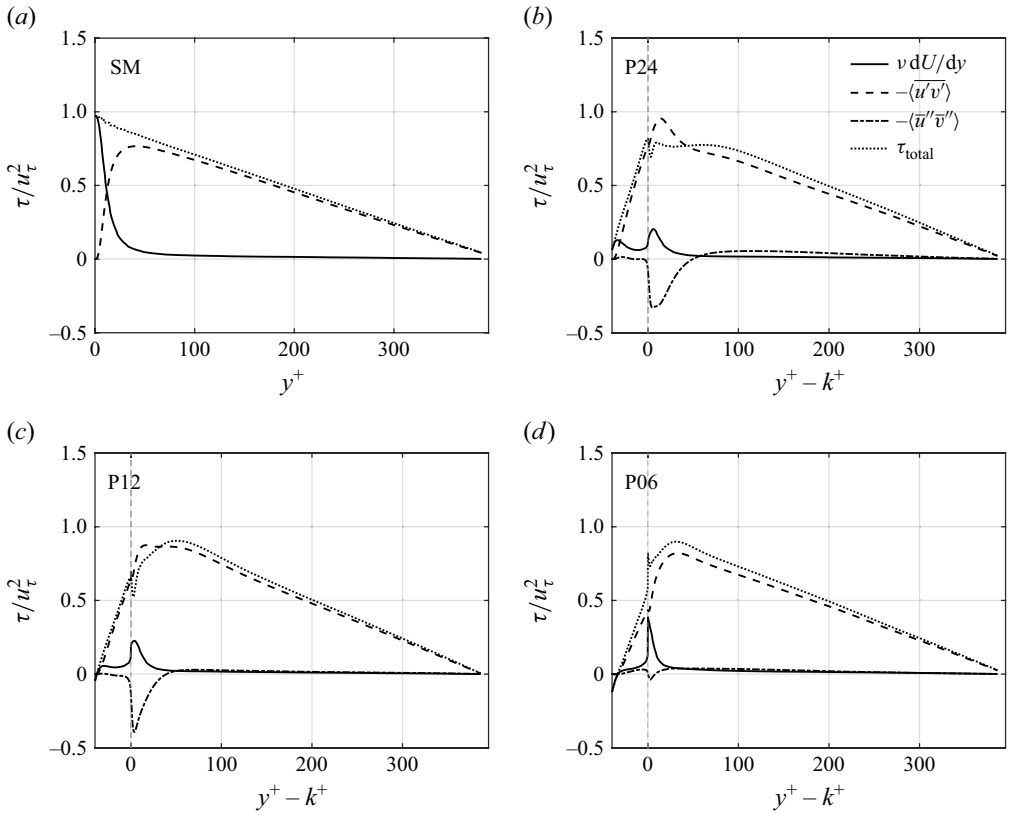


Figure 24. Stress decomposition profiles versus $y^+ - k^+$ for (*a*) SM, (*b*) P24, (*c*) P12 and (*d*) P06. The curves show the viscous stress τ_v^+ (solid line), the Reynolds shear stress τ_R^+ (dashed), the dispersive shear stress τ_D^+ (dot-dashed, rough-wall cases only), and the total stress τ_{total}^+ (dotted). The grey vertical line at $y^+ - k^+ = 0$ marks the roughness crest height. The legend shown in figure (*b*) applies to all plots.

are analysed, and the connections between these characteristics and the changes in momentum transfer and velocity gradient at the QC interface are investigated. Three key findings are obtained as follows. First, the internal flow characteristics of the QC on rough and smooth surfaces are similar, which is consistent with Townsend's outer-layer similarity hypothesis (Townsend 1976). Second, the roughness directly modifies the flow within the roughness sublayer, where the turbulence characteristics are closely tied to the element spacing, and these sublayer modifications are accompanied by systematic changes in the QC geometry, indicating that the influence of roughness extends into the outer layer rather than being confined to the inner region.

Finally, as a result of the changes in the roughness sublayer, the QC on rough surfaces exhibits characteristics of narrowing, more intense swaying, more frequent extension towards the wall, or central fragmentation compared with that over smooth surfaces. Specifically, the influences of different roughness configurations on the flow, as reflected by the changes in the geometric characteristics of the QC, are summarised as follows.

(i) Sparse (P24, $p/k = 24$): QC thinning and swaying are modest, and interface strengthening is moderate. Among the rough-wall cases, this configuration yields the smallest ΔU^+ and is closest to conditional outer-layer similarity.

https://doi.org/10.1017/jfm.2026.11950 Published online by Cambridge University Press

(ii) Intermediate (P12, $p/k = 12$): QC wall-normal variation is the strongest. The core is thinner than that on the smooth wall, but on average thicker than that of P24. Variances of δ_c and y_c are the largest. Near-wall QC occurrence is more frequent, and centreline intermittency is highest. The boundary approaches the wall more often, which yields the largest interfacial velocity jump and spanwise vorticity peak. The stronger shear induced by this velocity gradient leads to larger amplitudes of velocity fluctuations near the QC boundary, making the momentum transfer at this position dominated by larger fluctuations. This weakens the momentum transfer structure at the average position, thereby affecting the structural similarity. Correspondingly, the LSE-conditioned vortical structures at the QC boundary are the most spatially compact among all cases, and the conditioning event at the interface corresponds to the lowest probability density P_0 among the rough-wall cases, indicating a shift towards less probable, higher-amplitude events in the joint PDF. Therefore, the changes in similarity in this case mainly stem from (a) the intense wall-normal fluctuation of the QC, and (b) the increased shear caused by the fluctuation, which leads to changes in the momentum transfer structure. The results suggest that the drag increase is associated with the intensified fragmentation and wall-normal excursions of the QC, the principal momentum-containing region.

(iii) Dense (P06, $p/k = 6$): with the smallest element spacing, previous studies have shown that the influence of this roughness distribution outside the roughness sublayer is the closest to that of the smooth surface. The element array and its wake-induced mixing layer impose a near-planar imprint on the outer flow. Ejections lift and thin the QC. The QC is the thinnest, and y_c variability is moderate. The QC characteristics in the present study also show similar results: the stability of the geometric characteristics of the QC in this case is closest to that over a smooth surface, including the momentum transfer characteristics at the QC interface. Among the rough-wall cases, the LSE-conditioned structures at the QC boundary and the associated conditioning parameters remain closest to the smooth-wall reference, providing quantitative confirmation that the similarity in QC geometry is accompanied by a corresponding similarity in interfacial structural organisation. However, the difference lies in the fact that the presence of the roughness sublayer lifts the momentum transfer structure, causing it to penetrate deeper into the vicinity of the channel centre, and leading to the narrowing of the QC. Therefore, the changes in similarity and drag in this case originate from the narrowing of the main momentum-containing region.

From the perspective of the QC, the analysis of rough-wall channel flow is divided into three parts.

(i) Outside the QC. In this region, the flow is mainly affected by the roughness. Both the momentum transfer structure and magnitude are directly related to the arrangement of the roughness elements.

(ii) QC boundary position. The strong shear at the QC boundary is influenced by the geometric characteristics of the QC, and this strong shear in turn causes changes in the momentum transfer structure in this region.

(iii) Inside the QC. For different rough walls and smooth walls, the internal flow characteristics of the QC are consistent. However, since it contains the strongest streamwise momentum, changes in its geometric characteristics directly reflect the roughness drag and outer-layer similarity. That is, for the configurations examined here, QC narrowing and intensified wall-normal excursions are found to accompany

https://doi.org/10.1017/jfm.2026.11950 Published online by Cambridge University Press

increased roughness drag and departures from outer-layer similarity, suggesting that QC geometric deformation is associated with these flow responses.

The main analysis is conducted at $Re_\tau = 395$, and a limited comparison at $Re_\tau = 590$ presented in Appendix C suggests that the QC geometry statistics are insensitive to this moderate Reynolds number change for the P24 configuration, but the behaviour over a substantially wider range of Reynolds numbers, different roughness heights and 3-D topologies remains to be determined.

Funding. This work was supported by NSFC (grant nos 12225204, 12402254 and 12588201), the Department of Science and Technology of Guangdong Province (grants nos 2023B1212060001 and 2020B1212030001), and the Shenzhen Science and Technology Programme (grant no. SYSPG20241211173725008). Numerical simulations were supported by the Centre for Computational Science and Engineering of the Southern University of Science and Technology.

Declaration of interests. The authors report no conflict of interest.

Data availability statement. The data that support the findings of this study are available from the corresponding author upon reasonable request.

Appendix A. The PDF- and KDE-based UMZ identification: algorithms and comparison

This appendix documents the density-estimation procedures used to identify UMZs within a 3-D window and to determine the interfacial threshold u_k as the valley between adjacent modes. The physical motivation, window-sensitivity results and fixed-threshold strategy are presented in the main text (§ 4) and are not repeated here.

A.1 *Histogram-based PDF*

Within a chosen 3-D window spanning the full height, instantaneous velocities are normalised by the centreline value u/U_{CL}, and a PDF is formed by uniform binning. Local maxima of the PDF correspond to instantaneous modal velocities u_m, and the local minimum between neighbouring maxima defines the interfacial threshold u_k (Adrian *et al.* 2000; de Silva *et al.* 2016, 2017). To limit spurious modes due to bin sensitivity, standard peak-finding criteria (minimum separation, minimum height and minimum prominence) are applied; windows that do not satisfy these criteria (e.g. unimodal distributions during strong events) are treated as ambiguous for valley-based u_k.

Figure 25 illustrates the histogram-based identification for the same 3D window used in the main-text figure 5; panel (*b*) reproduces the corresponding velocity slice used for figure 5(*b*). Two modal velocities are recovered and the inter-modal valley yields $u_k \approx 0.88\,U_{CL}$ for this window, consistent with the KDE counterpart.

A.2 *Kernel density estimation*

Kernel density estimation constructs a continuous estimate of the PDF by placing a kernel function at each observation and summing the contributions, thereby avoiding the bin-edge sensitivity inherent in histogram-based approaches. To reduce binning sensitivity, a KDE is constructed from the same window samples $\{u_i/U_{CL}\}_{i=1}^{N}$. In statistical form,

$$\hat{f}(u) = \frac{1}{N\,b_w}\sum_{i=1}^{N} K\left(\frac{u-u_i}{b_w}\right), \tag{A1}$$

https://doi.org/10.1017/jfm.2026.11950 Published online by Cambridge University Press

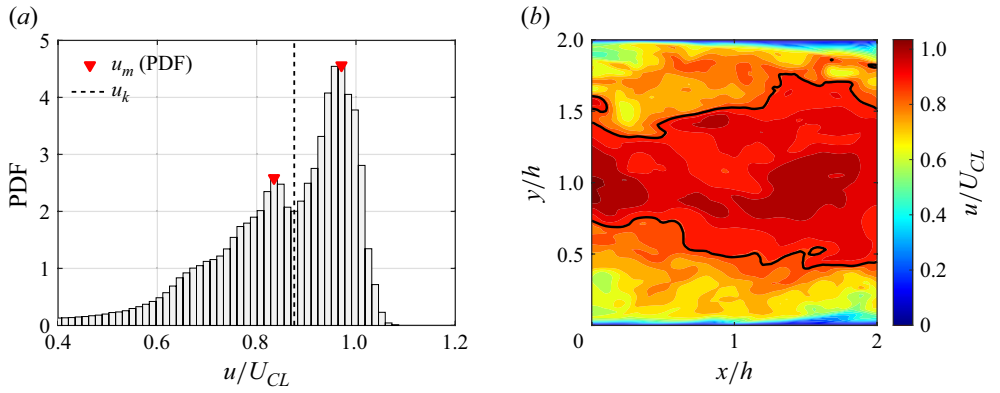


Figure 25. Histogram-based UMZ identification for the same 3-D window as the main text figure 5: (*a*) histogram PDF of u/U_{CL} with modal velocities (u_m) and the valley-based threshold (u_k); (*b*) identical velocity slice with the $u = u_k$ contour.

where $K(\cdot)$ is the kernel (typically Gaussian), and b_w is the bandwidth controlling smoothness. Modes are defined as the peaks of $\hat{f}(u)$, and modal velocities follow from their locations u_m. The interfacial threshold u_k is defined as the minimum of $\hat{f}(u)$ between adjacent modes. In practice, a Gaussian kernel is adopted, and b_w is determined following the optimal bandwidth formula of Scott (2011):

$$b_w = \hat{\sigma}\left(\frac{4}{3}\right)^{1/5} N^{-1/5}, \tag{A2}$$

where $\hat{\sigma}$ is the standard deviation of the window samples, which minimises the mean integrated squared error between $\hat{f}(u)$ and the true density (Fan *et al.* 2019). Bandwidths deviating from this value either merge adjacent modes (excessive smoothing) or introduce spurious peaks (insufficient smoothing).

A.3 *Method comparison*

When the histogram PDF exhibits well-separated modes, the KDE returns the same u_m and u_k within plotting accuracy. For noisier or weakly bimodal windows, the KDE remains stable and still identifies two modes and a valley, whereas the histogram may yield a shallow valley or a single peak. Two representative smooth-wall windows are shown in figure 26, where figure 26(*a*) illustrates close agreement, and figure 26(*b*) shows a challenging case where the KDE robustly recovers two modes and the corresponding u_k despite the shallow histogram valley. In practice, the histogram is useful as a diagnostic of binning artefacts, and the KDE is used to stabilise peak/valley identification.

Appendix B. The ISL thickness and the role of threshold selection

The QC is identified using a fixed threshold $U_k/U_{CL} = 0.95$ across all cases, as established in § 4.3 on the basis of the convergent modal velocity $U_{m,1}$. As noted there, the case-specific thresholds derived from the PDF valley (table 2) differ across roughness configurations, ranging from $U_k/U_{CL} = 0.90$ (P12) to $U_k/U_{CL} = 0.95$ (SM). A natural question is whether the adoption of a common threshold introduces a systematic bias through the partial inclusion of the ISL – the thin, highly sheared region bounding the QC – within the detected core region. This appendix estimates the ISL thickness δ_w for

https://doi.org/10.1017/jfm.2026.11950 Published online by Cambridge University Press

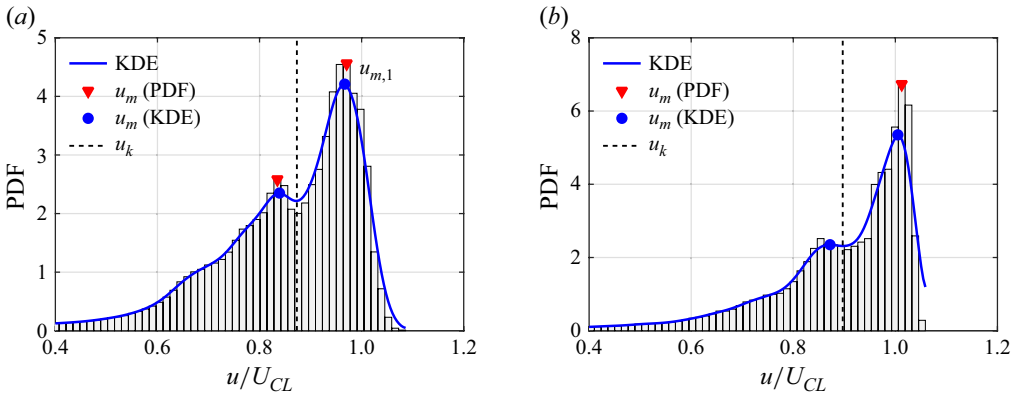


Figure 26. Comparison of histogram PDF (symbols) and KDE (solid blue) for two SM windows. The modal velocities from the histogram (red triangles) and KDE (blue circles), together with the valley-based threshold u_k (dashed), are shown.

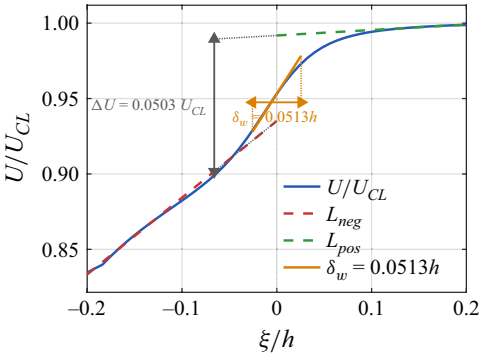


Figure 27. Illustration of the ISL thickness estimation procedure. The conditionally averaged streamwise velocity profile U_Σ/U_{CL} is shown as a function of the interface-relative coordinate ξ/h. Red and green dashed lines denote the linear fits applied in the regions $\xi/h < -\xi_{fit}$ and $\xi/h > \xi_{fit}$, respectively. Their extrapolated values at $\xi = 0$ define the velocity jump ΔU. The orange line segment indicates the maximum gradient $(\partial U_\Sigma/\partial\xi)_{max}$, and the horizontal double-headed arrow marks the resulting thickness δ_w (see (B1)).

each case, and discusses its implications for threshold selection, then examines directly the sensitivity of the principal QC geometry statistics to the threshold value.

The thickness δ_w is estimated following de Silva *et al.* (2017) and Gul *et al.* (2020). Using the interface-relative coordinate $\xi = y - y_I$ defined in (6.3), the streamwise velocity is conditionally averaged with respect to the instantaneous QC boundary y_I (taking both the upper and lower boundaries y_u and y_l in turn) to obtain the profile $U_\Sigma(\xi)$, following the interfacial averaging operation defined in (6.4). The procedure is illustrated in figure 27. Linear fits are applied to $U_\Sigma(\xi)$ in the regions $|\xi|/h > \xi_{fit}$ (with $\xi_{fit}/h = 0.12$), sufficiently far from the interface on either side, and the velocity jump ΔU is defined as the difference between the extrapolated values of these fits evaluated at $\xi = 0$. The ISL thickness is then defined as

$$\delta_w = \frac{\Delta U}{\left(\partial U_\Sigma/\partial\xi\right)_{max}}, \tag{B1}$$

https://doi.org/10.1017/jfm.2026.11950 Published online by Cambridge University Press

Case	$U_k/U_{CL}=0.90$		$U_k/U_{CL}=0.91$		$U_k/U_{CL}=0.93$		$U_k/U_{CL}=0.95$	
	$\Delta U/U_{CL}$	δ_w/h	$\Delta U/U_{CL}$	δ_w/h	$\Delta U/U_{CL}$	δ_w/h	$\Delta U/U_{CL}$	δ_w/h
SM	—	—	—	—	—	—	0.050	0.051
P24	0.136	0.070	0.134	0.072	0.131	0.076	0.127	0.079
P12	0.193	0.073	0.190	0.074	0.185	0.076	0.182	0.079
P06	0.151	0.076	0.149	0.077	0.146	0.080	0.142	0.084

Table 5. Velocity jump $\Delta U/U_{CL}$ and ISL thickness δ_w/h, for all cases at four threshold values U_k/U_{CL}. The thickness is computed from the conditionally averaged streamwise velocity profile following (B1), after de Silva *et al.* (2017) and Gul *et al.* (2020). Dashes indicate that a well-defined sharp transition could not be identified for the SM case at these thresholds.

where $(\partial U_\Sigma/\partial\xi)_{max}$ is the maximum wall-normal gradient of the conditionally averaged profile in the vicinity of $\xi=0$. This definition is equivalent to approximating the sharp velocity transition as a linear ramp of slope equal to the peak gradient, so that δ_w represents the wall-normal extent over which the velocity jump ΔU would occur at that maximum rate. The values of ΔU and δ_w reported below are averaged between the upper and lower interfaces.

Table 5 summarises $\Delta U/U_{CL}$ and δ_w/h for all cases. For the SM case, only the result at $U_k/U_{CL}=0.95$ is reported; at lower thresholds, the conditionally averaged profile does not exhibit a well-defined sharp transition, consistent with the comparatively weak and diffuse ISL in the smooth-wall flow.

The velocity jump ΔU is largest for case P12 across all threshold values examined, consistent with the conclusion in § 6.1 that P12 undergoes the strongest wall-normal excursions, bringing the QC boundary closer to the wall, and thereby producing the largest velocity contrast across the interface and the strongest spanwise vorticity peak Ω_z (figure 17*b*). Despite having the largest ΔU, P12 does not exhibit the largest δ_w: case P06 yields the greatest ISL thickness at every threshold, exceeding P12 by approximately 4–5 %, and P24 by approximately 7–8 %, in relative terms. This indicates that the velocity gradient within the shear layer is comparatively weaker in P06 than in P12, consistent with the structural broadening associated with the dense-roughness configuration described in § 7.

Most pertinent to the threshold question, the rough-wall cases (P24, P12, P06) all exhibit δ_w values substantially larger than the smooth-wall reference. At $U_k/U_{CL}=0.95$, the rough-wall values range from approximately $0.079h$ to $0.084h$, compared with $0.051h$ for SM – a relative excess of approximately 55–65 %. This disparity implies that a uniform reduction of U_k/U_{CL} below 0.95 would encroach upon the ISL to a greater extent in the rough-wall cases than in the smooth-wall case, disproportionately inflating the apparent core statistics of the rough-wall cases, and suppressing the inter-case contrasts. It should be noted that neither a uniform nor a case-specific threshold can fully exclude the ISL from the detected core region, given that the ISL occupies a finite wall-normal extent in all cases. However, the use of case-specific PDF-valley thresholds introduces an additional source of variability: since δ_w differs systematically across roughness configurations, each case-specific threshold absorbs a different fraction of the ISL, superimposing a configuration-dependent geometric bias onto the core statistics that is unrelated to the flow dynamics of interest. A uniform threshold $U_k/U_{CL}=0.95$, while subject to the same ISL contamination in an absolute sense, applies a consistent identification criterion across

https://doi.org/10.1017/jfm.2026.11950 Published online by Cambridge University Press

Case	U_k/U_{CL}	δ_c/h		y_c/h		$\gamma\ (y/h=1)$
		μ/h	σ/h	μ/h	σ/h	
SM	0.90	1.11	0.25	1.00	0.13	0.01
	0.91	1.05	0.26	1.00	0.14	0.01
	0.93	0.92	0.27	1.00	0.15	0.03
	0.95	0.79	0.27	1.00	0.16	0.08
P24	0.90	0.92	0.30	1.00	0.19	0.08
	0.91	0.88	0.31	1.00	0.19	0.18
	0.93	0.79	0.31	1.00	0.20	0.22
	0.95	0.71	0.31	1.00	0.21	0.26
P12	0.90	0.92	0.34	1.00	0.21	0.10
	0.91	0.88	0.34	1.00	0.21	0.20
	0.93	0.81	0.34	1.00	0.22	0.27
	0.95	0.73	0.34	1.00	0.23	0.31
P06	0.90	0.81	0.29	0.99	0.17	0.08
	0.91	0.77	0.29	0.99	0.18	0.15
	0.93	0.70	0.28	0.99	0.18	0.22
	0.95	0.63	0.28	0.99	0.19	0.26

Table 6. Sensitivity of the key QC geometry statistics to the threshold value U_k/U_{CL} for the smooth- and rough-wall cases. The mean (μ) and standard deviation (σ) are calculated from the respective PDFs of the core thickness δ_c and centre position y_c, while the intermittency factor γ is evaluated at the channel centreline ($y/h=1$). The values at $U_k/U_{CL}=0.95$ correspond to the uniform threshold used throughout the main text. The case-specific PDF-valley thresholds are 0.95, 0.93, 0.90 and 0.91 for SM, P24, P12 and P06, respectively.

all cases. To assess whether the principal QC statistics depend on this choice, table 6 summarises the corresponding values of δ_c, y_c and γ at the four thresholds examined.

Although the absolute values vary with the threshold, the principal inter-case distinctions are retained: the rough-wall cases exhibit a thinner QC, greater centre position variability and higher centreline intermittency than SM over the range examined. The conclusions presented in the main text are therefore not contingent on the specific threshold adopted.

Appendix C. Reynolds number and domain-length sensitivity

C.1 *Effect of Reynolds number*

Figure 28 shows the aggregated distributions of $u_{m,1}$ and $u_{m,2}$ for P24H. The first modal velocity peaks at $U_{m,1}/U_{CL}=1.00$, close to the P24 value, while the second modal velocity peaks at $U_{m,2}/U_{CL}=0.86$, slightly lower than the P24 value 0.89, with σ_2 increasing modestly from 0.10 to 0.11, as shown in table 2. The threshold obtained from the PDF valley is $U_k/U_{CL}=0.93$, the same as for P24. The insensitivity of $U_{m,1}$ and U_k to the change in Reynolds number is consistent with the observation of Kwon *et al.* (2014) that the QC threshold velocity is approximately independent of Reynolds number in smooth-wall channel flows. On this basis, the fixed threshold $U_k/U_{CL}=0.95$ is also applied to P24H in the present study.

Figures 29(a) and 29(b) compare the QC geometry statistics of P24 and P24H. The PDFs of δ_c in figure 29(a) exhibit similar distribution shapes for the two cases, with mean values differing by approximately $0.01h$ ($\mu/h=0.71$ for P24, and $\mu/h=0.70$ for P24H),

https://doi.org/10.1017/jfm.2026.11950 Published online by Cambridge University Press

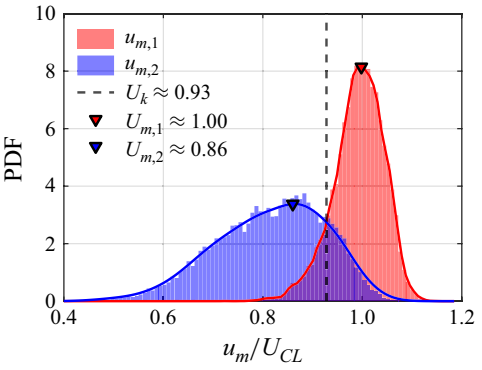


Figure 28. Aggregated PDFs of the first ($u_{m,1}$, red) and second ($u_{m,2}$, blue) modal velocities for P24H ($Re_\tau = 590$).

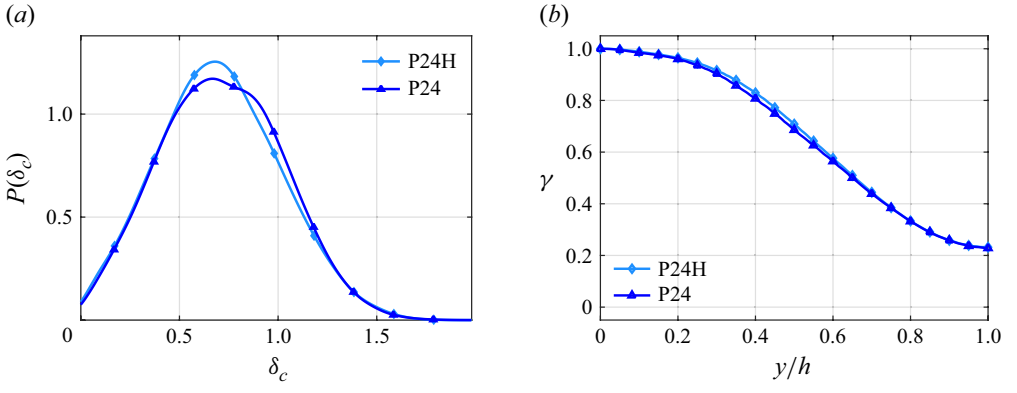


Figure 29. Comparison of QC geometry statistics between P24 ($Re_\tau = 395$) and P24H ($Re_\tau = 590$). (*a*) The PDFs of the core thickness δ_c. (*b*) Profiles of the intermittency factor γ as a function of the wall-normal position y/h.

and standard deviation $0.31h$ for both. The intermittency profiles $\gamma(y/h)$ in figure 29(*b*) remain close across the channel height, with both cases yielding $\gamma = 0.26$ at the centreline, as shown in table 3. The centre position statistics are likewise similar and are summarised in table 3.

Over the two Reynolds numbers $Re_\tau = 395$ and 590, the QC geometric statistics of P24 and P24H show limited variation for this roughness configuration. It should be noted that this comparison is based on a single roughness geometry at two Reynolds numbers, and does not constitute a general characterisation of Reynolds number effects on the QC. The behaviour of the QC geometry over a wider range of Reynolds numbers and for other roughness configurations remains to be established.

C.2 *Streamwise domain convergence for case P24*

To assess the sensitivity of the QC statistics to streamwise domain length, an additional simulation was performed with the P24 geometry at doubled extent, $L_x = 24h$ (case P24L), with all other parameters identical to P24. Figure 30 shows the mean velocity

https://doi.org/10.1017/jfm.2026.11950 Published online by Cambridge University Press

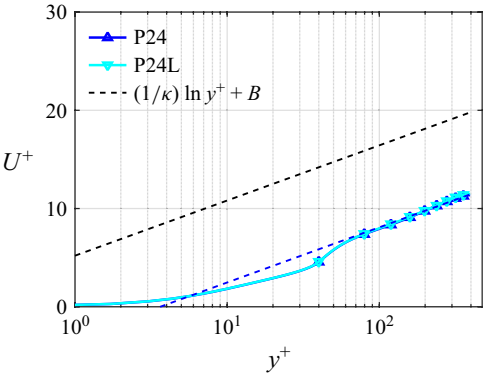


Figure 30. Comparison of mean velocities between P24 ($L_x = 12h$) and P24L ($L_x = 24h$).

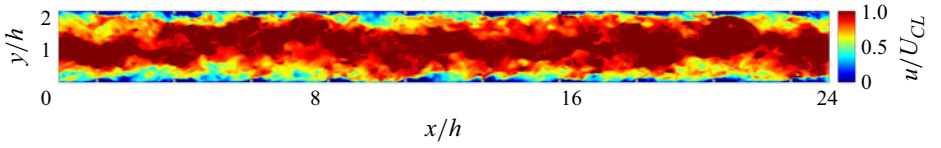


Figure 31. Instantaneous contour of u/U_{CL} in an x–y plane for case P24L ($L_x = 24h$). The solid black line denotes the QC boundary defined at the threshold $u/U_{CL} = 0.95$.

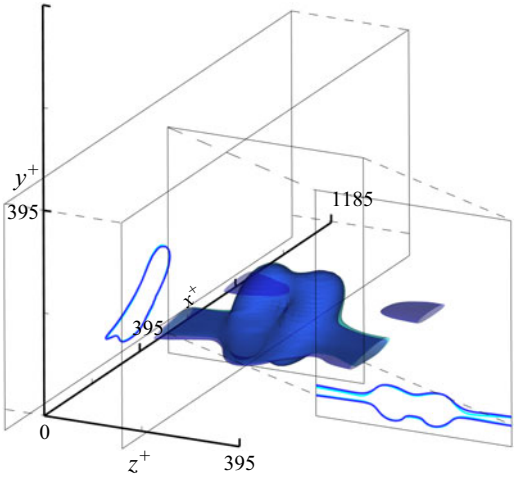


Figure 32. Comparison of LSE-conditioned Q2 vortical structures at $y^+ \approx 47$ for P24 ($L_x = 12h$, blue) and P24L ($L_x = 24h$, cyan).

profiles for P24 and P24L. The two cases are in close agreement across the full wall-normal range, indicating that the bulk flow statistics are not materially affected by the streamwise domain length. Figure 31 shows an instantaneous contour of u/U_{CL} for P24L, with the QC boundary at $u/U_{CL} = 0.95$; the boundary topology is qualitatively similar to that of P24. Figure 32 compares the LSE-conditioned Q2 vortical structures at $y^+ \approx 47$ for P24 and P24L. The primary hairpin structure above the roughness crests is

https://doi.org/10.1017/jfm.2026.11950 Published online by Cambridge University Press

broadly consistent between the two cases. A difference is apparent within the inter-element cavities, where the periodic wakes are more fully developed in P24L owing to the greater number of pitch repetitions N_p in the longer domain. This reflects a modest limitation of the $L_x = 12h$ configuration in resolving near-element wake structures. The structures above the roughness sublayer, which are the primary focus of the QC analyses in the main text, show no substantial difference between the two domain lengths.

References

Adrian, R.J. 1996 Stochastic estimation of the structure of turbulent fields. In *Eddy Structure Identification* (ed. J.P. Bonnet), pp. 145–195. Springer.

Adrian, R.J., Meinhart, C.D. & Tomkins, C.D. 2000 Vortex organization in the outer region of the turbulent boundary layer. *J. Fluid Mech.* **422**, 1–54.

Asadi, M., Kamruzzaman, M. & Hearst, R.J. 2022 The effect of inlet turbulence on the quiescent core of turbulent channel flow. *J. Fluid Mech.* **935**, A37.

Chen, X., Chung, Y.M. & Wan, M. 2020 Uniform-momentum zones in a turbulent pipe flow. *J. Fluid Mech.* **884**, A25.

Chen, X., Chung, Y.M. & Wan, M. 2021 The uniform-momentum zones and internal shear layers in turbulent pipe flows at Reynolds numbers up to $Re_\tau = 1000$. *Intl J. Heat Fluid Flow* **90**, 108817.

Cheng, C., Chen, X., Zhu, W., Shyy, W. & Fu, L. 2024 Progress in physical modeling of compressible wall-bounded turbulent flows. *Acta Mechanica Sin.* **40** (1), 323663.

Christensen, K.T. & Adrian, R.J. 2001 Statistical evidence of hairpin vortex packets in wall turbulence. *J. Fluid Mech.* **431**, 433–443.

Chung, D., Hutchins, N., Schultz, M.P. & Flack, K.A. 2021 Predicting the drag of rough surfaces. *Annu. Rev. Fluid Mech.* **53** (1), 439–471.

Clauser, F.H. 1954 Turbulent boundary layers in adverse pressure gradients. *J. Aeronaut. Sci.* **21** (2), 91–108.

Fan, D., Xu, J., Yao, M.X. & Hickey, J.-P. 2019 On the detection of internal interfacial layers in turbulent flows. *J. Fluid Mech.* **872**, 198–217.

Fischer, P.F., Lottes, J.W. & Kerkemeier, S.G. 2008 nek5000 web page. Mathematics and Computer Science Division, Argonne National Laboratory. Available at: https://nek5000.mcs.anl.gov (accessed 31 July 2024).

Flack, K.A. & Schultz, M.P. 2014 Roughness effects on wall-bounded turbulent flows. *Phys. Fluids* **26** (10), 101305.

Guerrero, B., Lambert, M.F. & Chin, R.C. 2023 Transient behaviour of decelerating turbulent pipe flows. *J. Fluid Mech.* **962**, A44.

Gul, M., Elsinga, G.E. & Westerweel, J. 2020 Internal shear layers and edges of uniform momentum zones in a turbulent pipe flow. *J. Fluid Mech.* **901**, A10.

Han, J., Zhang, W., Zhang, L. & Wan, M. 2026 Turbulent flow and mixing layer over large two-dimensional square roughness. *Acta Mechanica Sin.* **42** (2), 325088.

Hearst, R.J., de Silva, C.M., Dogan, E. & Ganapathisubramani, B. 2021 Uniform-momentum zones in a turbulent boundary layer subjected to freestream turbulence. *J. Fluid Mech.* **915**, A109.

Heisel, M., de Silva, C.M., Hutchins, N., Marusic, I. & Guala, M. 2020 On the mixing length eddies and logarithmic mean velocity profile in wall turbulence. *J. Fluid Mech.* **887**, R1.

Jiménez, J. 2004 Turbulent flows over rough walls. *Annu. Rev. Fluid Mech.* **36** (1), 173–196.

Jin, Y., Uth, M.-F. & Herwig, H. 2015 Structure of a turbulent flow through plane channels with smooth and rough walls: an analysis based on high resolution DNS results. *Comput. Fluids* **107**, 77–88.

Kevin, K., Monty, J. & Hutchins, N. 2019 The meandering behaviour of large-scale structures in turbulent boundary layers. *J. Fluid Mech.* **865**, R1.

Kong, J., Bennetts, L.G., Nugroho, B. & Chin, R.C. 2023 Systematic study of the Reynolds number and streamwise spacing effects in two-dimensional square-bar rough-wall turbulent boundary layers. *Phys. Rev. Fluids* **8** (1), 014601.

Krogstad, P.-Å. & Efros, V. 2012 About turbulence statistics in the outer part of a boundary layer developing over two-dimensional surface roughness. *Phys. Fluids* **24** (7), 075112.

Kwon, Y.S., Philip, J., de Silva, C.M., Hutchins, N. & Monty, J.P. 2014 The quiescent core of turbulent channel flow. *J. Fluid Mech.* **751**, 228–254.

Leonardi, S., Orlandi, P., Djenidi, L. & Antonia, R.A. 2004 Structure of turbulent channel flow with square bars on one wall. *Intl J. Heat Fluid Flow* **25** (3), 384–392.

Leonardi, S., Orlandi, P., Smalley, R.J., Djenidi, L. & Antonia, R.A. 2003 Direct numerical simulations of turbulent channel flow with transverse square bars on one wall. *J. Fluid Mech.* **491**, 229–238.

https://doi.org/10.1017/jfm.2026.11950 Published online by Cambridge University Press

LU, S.S. & WILLMARTH, W.W. 1973 Measurements of the structure of the Reynolds stress in a turbulent boundary layer. *J. Fluid Mech.* **60** (3), 481–511.

MACDONALD, M., CHAN, L., CHUNG, D., HUTCHINS, N. & OOI, A. 2016 Turbulent flow over transitionally rough surfaces with varying roughness densities. *J. Fluid Mech.* **804**, 130–161.

MACDONALD, M., OOI, A., GARCÍA-MAYORAL, R., HUTCHINS, N. & CHUNG, D. 2018 Direct numerical simulation of high aspect ratio spanwise-aligned bars. *J. Fluid Mech.* **843**, 126–155.

PERRY, A.E., SCHOFIELD, W.H. & JOUBERT, P.N. 1969 Rough wall turbulent boundary layers. *J. Fluid Mech.* **37** (2), 383–413.

POPE, S.B. 2000 *Turbulent Flows*. Cambridge University Press.

RAUPACH, M.R., ANTONIA, R.A. & RAJAGOPALAN, S. 1991 Rough-wall turbulent boundary layers. *Appl. Mech. Rev.* **44** (1), 1–25.

SALESKY, S.T. 2023 Uniform momentum and temperature zones in unstably stratified turbulent flows. *J. Fluid Mech.* **958**, A7.

SCOTT, D.W. 2011 Multivariate density estimation and visualization. In *Handbook of Computational Statistics: Concepts and Methods* (ed. J.E. Gentle, W.K. Härdle & Y. Mori), pp. 549–569. Springer.

DE SILVA, C.M., HUTCHINS, N. & MARUSIC, I. 2016 Uniform momentum zones in turbulent boundary layers. *J. Fluid Mech.* **786**, 309–331.

DE SILVA, C.M., PHILIP, J., HUTCHINS, N. & MARUSIC, I. 2017 Interfaces of uniform momentum zones in turbulent boundary layers. *J. Fluid Mech.* **820**, 451–478.

SQUIRE, D.T., MORRILL-WINTER, C., HUTCHINS, N., SCHULTZ, M.P., KLEWICKI, J.C. & MARUSIC, I. 2016 Comparison of turbulent boundary layers over smooth and rough surfaces up to high Reynolds numbers. *J. Fluid Mech.* **795**, 210–240.

TANI, I. 1987 Turbulent boundary layer development over rough surfaces. In *Perspectives in Turbulence Studies* (ed. H.U. Meier & P. Bradshaw), pp. 223–249. Springer.

TOWNSEND, A.A.R. 1976 *The Structure of Turbulent Shear Flow*. Cambridge University Press.

VANDERWEL, C. & GANAPATHISUBRAMANI, B. 2019 Turbulent boundary layers over multiscale rough patches. *Boundary-Layer Meteorol.* **172** (1), 1–16.

VOLINO, R.J., SCHULTZ, M.P. & FLACK, K.A. 2009 Turbulence structure in a boundary layer with two-dimensional roughness. *J. Fluid Mech.* **635**, 75–101.

VOLINO, R.J., SCHULTZ, M.P. & FLACK, K.A. 2011 Turbulence structure in boundary layers over periodic two- and three-dimensional roughness. *J. Fluid Mech.* **676**, 172–190.

WANG, X., GUO, J., WANG, J. & CHEN, S. 2024 Interfaces of high- and low-speed large-scale structures in compressible turbulent mixing layers: compressibility effects and structures. *J. Fluid Mech.* **981**, A6.

WANG, Y.-F., HUANG, Y.-J., ZHANG, J.-H., TIAN, H.-P. & JIANG, N. 2023 Uniform momentum zones on the smooth and superhydrophobic surfaces in a turbulent boundary layer. *Acta Mechanica Sin.* **39** (8), 322467.

YANG, J., HWANG, J. & SUNG, H.J. 2016 Structural organization of the quiescent core region in a turbulent channel flow. *Intl J. Heat Fluid Flow* **62**, 455–463.

ZHANG, Z., FENG, Z., HUO, K. & JIANG, N. 2026 Outer-layer similarity from the perspective of uniform momentum zones in turbulent boundary layer over smooth and rough wall. *Intl J. Heat Fluid Flow* **119**, 110292.

ZHOU, J., ADRIAN, R.J., BALACHANDAR, S. & KENDALL, T.M. 1999 Mechanisms for generating coherent packets of hairpin vortices in channel flow. *J. Fluid Mech.* **387**, 353–396.

https://doi.org/10.1017/jfm.2026.11950 Published online by Cambridge University Press